

1 **The anatomy of exhumed river-channel belts: Bedform- to belt-scale river kinematics of the**
2 **Ruby Ranch Member, Cretaceous Cedar Mountain Formation, Utah, USA**

3 Benjamin T. Cardenas^{1,2*}, David Mohrig¹, Timothy A. Goudge¹, Cory M. Hughes³, Joseph S. Levy⁴,
4 Travis Swanson⁵, Jasmine Mason¹, and Feifei Zhao¹

5 ¹Jackson School of Geosciences, University of Texas at Austin, Austin, TX, USA

6 ²now at the Division for Geological and Planetary Sciences, California Institute of Technology,
7 Pasadena, CA, USA

8 ³Department of Geology, Western Washington University, Bellingham, WA, USA

9 ⁴Department of Geology, Colgate University, Hamilton, NY, USA

10 ⁵Department of Geology and Geography, Georgia Southern University, Statesboro, GA, USA

11

12 *Corresponding Author Contact Information

13 Telephone: (210) 240-0382

14 Email: bencard@caltech.edu

15 Re-submitted to Sedimentology after 2 rounds of revisions

16 Manuscript #: SED-2019-OM-199.R2

17

18 Word Count: 7,677 (8,000 limit)

19 Abstract: 242 (300 word limit)

20 Figures: 20

21 References: 112

THIS IS A PRE-PRINT THAT HAS NOT YET
COMPLETED THE PEER-REVIEW PROCESS

22 **ABSTRACT**

23 Many published interpretations of ancient fluvial systems have relied on observations of
24 extensive outcrops of thick successions. This paper, in contrast, demonstrates that a regional
25 understanding of paleoriver kinematics, depositional setting, and sedimentation rates can be
26 interpreted from local sedimentological measurements of bedform and barform strata. Dune
27 and bar strata, channel planform geometry, and bed topography are measured within exhumed
28 fluvial strata exposed as ridges in the Ruby Ranch Member of the Cretaceous Cedar Mountain
29 Formation, Utah, USA. The ridges are composed of lithified stacked channel belts, representing
30 at least 5 or 6 reoccupations of a single-strand channel. Lateral sections reveal well-preserved
31 barforms constructed of subaqueous dune cross sets. The topography of paleobarforms is
32 preserved along the top surface of the outcrops. Comparisons of the channel-belt centerline to
33 local paleotransport directions indicate channel planform geometry was preserved through the
34 re-occupations, rather than being obscured by lateral migration. Rapid avulsions preserved the
35 state of the active channel bed and its individual bars at the time of abandonment. Inferred
36 minimum sedimentation durations for the preserved elements, inferred from cross-set
37 thickness distributions and assumed bedform migration rates, vary within a belt from one to
38 ten days. Using only these local sedimentological measurements, the depositional setting is
39 interpreted as a fluvial megafan, given the similarity in river kinematics. This paper provides a
40 systematic methodology for the future synthesis of vertical and planview data, including the
41 drone-equipped 2020 Mars Rover mission to exhumed fluvial and deltaic strata.

42 **Keywords:** fluvial sedimentology, channel belt, preservation, bar, sinuous ridge

43

44 **INTRODUCTION**

45 Fluvial channel belts are the record of bedform and barform migration and
46 accumulation. Lateral migration, aggradation, and degradation of an ancient river is recorded
47 by the accumulations and bounding surfaces associated with these bedforms and bars, which in
48 turn make up the channel belts (Van De Lagewag et al., 2013). Therefore, in order to determine
49 the kinematics of ancient rivers, that is, how they migrated, aggraded, and avulsed, it is
50 necessary to understand the accumulation and preservation of the bedform and barform strata
51 within the associated channel belts (e.g., Reesink et al., 2015; Durkin et al., 2018; Paola et al.,
52 2018; Chamberlin and Hajek, 2019). Furthermore, variables such as water and sediment
53 discharge of an ancient fluvial system can only be determined if hydraulic geometries can be
54 accurately estimated from channel belts (Wright and Parker, 2003; Parker et al., 2007; Hayden
55 et al., 2019).

56 This paper examines an exhumed complex of fluvial deposits in the Ruby Ranch Member
57 of the Cretaceous Cedar Mountain Formation, Utah, USA (Fig. 1). The goal is to use local
58 sedimentological measurements of dune and bar strata to infer the regional kinematics and
59 depositional settings of the formative rivers. Here, new methodologies are developed for
60 extracting river-channel kinematics from channel-belt deposits. The measurements presented
61 here cover the channel belts across a range of scales, from local stacks of cross sets to entire
62 outcrops, in order to interpret the ancient river systems of the Ruby Ranch Member. The
63 datasets analyzed in this paper include aerial images collected from a drone, field maps, vertical

64 and lateral sections, and modern river analogs. The spread of paleotransport directions along
65 ridgetops is compared to modern rivers to understand the degree of lateral migration recorded
66 by the belts. Timescales related to the vertical aggradation of channel belts are constrained
67 using climb angles inferred from cross-set thickness distributions. Preserved bar topography is
68 identified by cross-set bounding surfaces that conform to the modern topography, and is
69 relevant for understanding avulsions and channel abandonment.

70

71 **Background**

72 *Ruby Ranch Member, Cedar Mountain Formation*

73 The rivers that deposited the Ruby Ranch Member of the Lower Cretaceous Cedar
74 Mountain Formation drained the uplifted Sevier thrust belt, in what is now modern-day
75 western Utah, northeastward towards the Mowry Sea and its successor, the Western Interior
76 Seaway (Currie, 1998, 2002). Ultimately, foreland-basin subsidence led to the burial of the
77 Cedar Mountain Formation by late Cretaceous coastal and marine deposits of the Naturita
78 Formation (formerly the Dakota Sandstone; Young, 1960; Carpenter, 2014) and the Mancos
79 Shale (Currie, 1998, 2002). A regional unconformity separates the base of the Cedar Mountain
80 Formation from the top of the upper Jurassic Morrison Formation (Peterson and Ryder, 1975;
81 Kowallis et al., 1986). The Ruby Ranch Member has been interpreted as consisting of channel
82 sandstones and conglomerates, and overbank mudstones and paleosols (Stokes, 1961; Currie,
83 1998; Garrison et al., 2007; Ludvigson et al., 2015; Nuse, 2015; Hayden et al., 2019).

84 The Cedar Mountain Formation is an important source of paleontological, climatic, and
85 tectonic information (Heller and Paola, 1989; Currie, 1998, 2002; Kirkland et al., 1999;
86 Ludvigson et al., 2010, 2015; Joeckel et al., 2017, 2019). Recent work regarding the Ruby Ranch
87 Member of the Cedar Mountain Formation has focused on the geomorphology of exhumed
88 channel deposits, which are more resistant than the surrounding floodplain material, resulting
89 in the preferential erosion of floodplain strata and preservation of the channel deposits that
90 form ridges (Williams et al., 2007; 2009; Hayden et al., 2019). These ridges are as tall as 35 m
91 and 60-90 m wide on average, and expose channel belts in three dimensions (Fig. 1). Recent
92 interest in these landforms and other exhumed channel belts (e.g., Hayden et al., 2019; in
93 Oman, Maizels 1987, 1990; Maizels and McBean, 1990; in Egypt, Zaki et al., 2018) has partially
94 been driven by high-resolution images of morphologically similar ‘fluvial sinuous ridges’ on
95 Mars (e.g., Burr et al., 2009; Davis et al., 2016; Cardenas et al., 2018; Hughes et al., 2019).
96 Hayden et al. (2019) have provided an important comparison between field- and remote-
97 sensing-based paleohydraulic reconstructions for the exhumed channel belts of the Ruby Ranch
98 Member, but the sedimentologic analysis herein provides additional information for
99 paleoenvironmental analysis.

100

101 *Dune, bar, and channel belt strata*

102 The dip direction of a dune cross stratum records the orientation of the formative dune
103 lee face, and reflects the local direction of dune migration (Allen, 1970; Rubin and Hunter,
104 1982). This relationship, however, is complicated in trough cross strata created by dunes with

105 sinuous crestlines (McKee and Weir, 1953; DeCelles et al., 1983; Rubin, 1987; Slingerland and
106 Williams, 1979). The local dip direction of a set of trough cross-stratification may represent the
107 mean migration direction of the associated dune plus or minus as much as 90° (Dott Jr., 1973;
108 Almeida et al., 2016). In plan-view exposures, the net migration direction can be determined
109 reliably, as well as the orientation of the bar surface the dune migrated on (Dott Jr., 1973;
110 Almeida et al., 2016). In channel deposits, larger dipping strata composed of smaller dune cross
111 sets, called compound strata, represent the accretion surfaces of barforms built by
112 superimposed dunes (Allen, 1983; Haszeldine, 1983; Edwards et al., 1983; Miall, 1985, 1988;
113 Almeida et al., 2016; Reesink, 2019).

114 Barforms are either fixed in position by channel shape or are free to migrate
115 downstream, although these represent end members of a continuum (Miall, 1977; Seminara
116 and Tubino, 1989; Ikeda, 1989; Hooke and Yorke, 2011). Point bars fixed to the inner bank of a
117 channel bend grow into the channel (Ikeda et al., 1981) and record lateral river migration. Point
118 bars have been identified in the rock record based on lateral accretion surfaces dipping towards
119 a range of orientations relative to the local dip directions of dune cross strata (e.g., Edwards et
120 al., 1983; Wu et al., 2015; Almeida et al., 2016). Free bars are able to migrate downstream,
121 though they may be attached to banks, and preserve a wider array of relationships between
122 local dune migration direction and the bar surface dip direction (e.g., Allen, 1983; Almeida et
123 al., 2016). Free bars and point bars commonly coexist in channels and in mixed-case forms (Fig.
124 2) (Kinoshita and Miwa, 1974; Whiting and Dietrich, 1993; Hooke and Yorke, 2011). Strata
125 representing both point bars and free bars may therefore be observed in the Ruby Ranch
126 Member.

127 In net-depositional settings, aggradation of the riverbed is coupled with aggradation of
128 the channel levees and proximal floodplain, and occurs more rapidly than in the distal
129 floodplain (Pizzuto, 1987). Over time, the channel becomes elevated relative to the floodplain,
130 and the difference between the two elevations defines the channel's superelevation. Past
131 studies have shown that a superelevation of 60% of the flow depth is linked to a threshold for
132 river avulsion (Mohrig et al., 2000), the process by which flow abandons a channel in favor of a
133 lower topographic pathway (Heller and Paola, 1996; Mohrig et al., 2000; Hajek and Edmonds,
134 2014; Chadwick, 2020). Studies of both modern and ancient avulsive rivers suggest that rivers
135 tend to return to previously abandoned channels that became attractors to flow following the
136 aggradation of the adjacent floodplain (Heller and Paola, 1996; Reitz et al., 2010; Edmonds et
137 al., 2016). Such systems leave behind channel-belt complexes, that is, stacked channel-belts
138 (Friend, 1979; Mohrig et al., 2000; Jones and Hajek, 2007; Cuevas Martínez et al., 2010;
139 Chamberlin and Hajek, 2015; Hayden et al., 2019).

140

141 **Modern-analog rivers**

142 Two modern rivers representing end-member braided and meandering planforms, the
143 North Loup River (Nebraska, USA) and Trinity River (Texas, USA), are used for comparisons in
144 this study. The North Loup River is a sand-bed braided river that has been used before as a
145 modern analog to ancient fluvial strata (Mohrig et al., 2000; Mahon and McElroy, 2018 The
146 North Loup River represents a reasonable analog to understand bar and bedform processes
147 occurring in the formative channels of the Ruby Ranch Member, as widths and depths are

148 similar. The eastern and western ridges are 63 and 90 m wide on average. The North Loup River
149 is 111 m wide in the studied reach, and ~1 – 1.5 m deep (Mohrig and Smith, 1996; Hayden et
150 al., 2019).). This study also uses analyzed bedforms and bars in the meandering Trinity River
151 (Mason and Mohrig, 2018; 2019a and b; Mason, 2018). The Trinity River has a similar width to
152 the ancient rivers described here (122 m on average), but is deeper. The similar widths are
153 significant for the aspects of this study focusing on the steering of dunes by bars.

154

155 **METHODS**

156 **Field measurements**

157 Several datasets were acquired at two adjacent ridges in the Ruby Ranch Member that
158 appear to have once been continuous (Fig. 1A and B). The ridges have good and accessible
159 sidewall and planview exposures. None of the normal faults mapped in the area appear to
160 intersect these ridges (Sable, 1956; Hayden et al., 2019). Aerial photosurveys, collected with a
161 DJI Phantom 2 Vision Plus drone, imaged the top and side surfaces of both ridges with >75%
162 along-path and side overlap in photos (Fig. 1C-D). Flights were conducted at 15-20 m above
163 ground level. Ground control point locations were determined using an Archer Field PC with an
164 external GPS antenna, producing horizontal position data with <0.3 m RMS accuracy.
165 Orthomosaics were generated with 5 cm spatial resolution using Agisoft Photoscan Pro
166 (www.agisoft.com), and cover an area of 213,000 m² over the eastern and western ridges (Fig.
167 1C to D). These datasets were used to map the locations of bounding surfaces of cross-sets and
168 major erosional surfaces. Dip directions of cross-strata identified on the photomosaics were

169 measured in the field using compasses. Each set was classified as either being composed of
170 sandstone or conglomerate.

171 Around the perimeters of each ridge, 59 vertical sections were measured covering the
172 entirety of the available vertical exposure of the ridge-top fluvial strata, resulting in 276 total
173 meters of section. An additional 31 2-D lateral sections ranging from 1 m to 10 m wide were
174 collected around the perimeters of both ridges in order to characterize the smaller, cross-set
175 scale architectural elements of the channel belts. Architectural variability in the transport
176 direction at the scale of a few meters was recorded, including changes in set thickness and the
177 dips of bounding surfaces. Across all of these surveys, the thickness of 362 sets of cross strata
178 were measured, and grain size was measured for 75 of those sets in the field using a SciOptic
179 translucent grain-size chart. Using a geographic information system (GIS), field mapping results
180 were merged with the remote sensing measurements. Ridge-scale bounding surfaces were
181 digitized as lines, and 1,071 sets of planform-exposed trough cross strata and 107 exposures of
182 large-scale dipping strata were digitized as polygons.

183

184 **Transport anomaly**

185 To test how well the ridge outcrop centerlines represent original channel centerlines, a
186 new metric is developed and named here as the *transport anomaly*, θ_{TA} . It is defined for both
187 modern rivers and the exhumed channel belts.

$$188 \quad \theta_{TA-CHANNEL} = \theta_{CL-CHANNEL} - \theta_{D-CHANNEL} \quad (1a)$$

189
$$\Theta_{TA-RIDGE} = \Theta_{CL-RIDGE} - \Theta_{D-RIDGE} \quad (1b)$$

190 where Θ_D is the 0 – 359° orientation of a transport or paleotransport measurement from an
191 active dune ($\Theta_{D-CHANNEL}$; Eq. 1a) or cross set ($\Theta_{D-RIDGE}$; Eq. 1b), and Θ_{CL} is the orientation of the
192 centerline nearest to the location where Θ_D was measured (Fig. 3). Values of Θ_{TA} may be
193 positive or negative, and are calculated using the Circular Statistics Toolbox available for
194 MATLAB (www.mathworks.com), which measures the shortest angular distance, positive or
195 negative, between the two directions such that no measurement exceeds 180° or is less than -
196 180° (Berens, 2009).

197 By measuring $\Theta_{D-CHANNEL}$ from dunes in modern rivers and $\Theta_{TA-RIDGE}$ from planform-
198 exposed cross sets in the Ruby Ranch Member, hundreds of measurements of Θ_{TA} (Eq. 1a to b)
199 between the ancient and modern systems were compared to test whether the transport
200 anomalies for the outcrop are distinct from transport anomalies observed in a modern river
201 system. To perform this comparison, Ruby Ranch Member ridge centerline trends and
202 paleotransports are required, as well as modern river centerlines and instantaneous transport
203 directions collected from dune crest orientations. The braided North Loup River and the
204 meandering Trinity River are used as the modern analogs.

205 This test assesses how well the centerlines of the ancient rivers are preserved in the
206 exhumed channel belts and represent ridge geometry (Fig. 4A and B). For example, if the mean
207 and standard deviation (σ) of $\Theta_{TA-RIDGE}$ (Eq. 1b) approximately equal those of $\Theta_{TA-CHANNEL}$ (Eq. 1a),
208 then the transport anomaly of the ancient deposit is no greater than the variability in a modern
209 river, and is consistent with channel-belt planform preserving the formative channel planform

210 (Fig. 4A). If lateral migration and reworking has greatly widened the channel belt and reduced
211 its overall sinuosity from that of the formative channels, σ should be greater in the ancient
212 deposit, as well as a more random distribution of $\theta_{TA-RIDGE}$ (Fig. 4B). An example of the latter
213 case comes from point bar strata of the Cretaceous Ferron Sandstone, Utah, USA, in Wu et al.,
214 (2015, their Fig. 13; 2016, their Fig. 8), who present a general northwest-curving paleotransport
215 trend along a northeast trending exposure, making their study location a high paleotransport
216 anomaly zone. Furthermore, the deviation angle in Wu et al. (2016) is calculated relative to an
217 interpreted channel-form, not the exhumed channel-belt shape. Wang and Bhattacharya (2017,
218 their Fig. 10A) show an even clearer example linked to point bar growth. Examples of this kind
219 of lateral amalgamation has been documented in both the ancient (Cretaceous McMurray
220 Formation, Alberta, Canada) and the modern (Mississippi River, Missouri and Arkansas, USA) by
221 Durkin et al. (2018). In a third scenario where erosion patterns have not exhumed the belt
222 evenly from all directions, the characteristics of both of the two aforementioned scenarios
223 would not be observed.

224 Points defining the centerlines of rivers were calculated using the series of points used
225 to define enclosing channel banks. For each point on one bank or ridge edge, the distance to
226 the nearest point on the opposite bank or ridge edge is calculated and taken as a local width
227 measurement, and a centerline point is placed at the location exactly between the two points.
228 The sequence of points spanning the length of the ridges or a river reach was smoothed using a
229 spline method in the MATLAB curve fitting toolbox. Centerlines are ultimately defined as points
230 spaced ~ 1 m apart along the smoothed line.

231 To measure local transport directions in the analog rivers, the brink lines of modern
232 dunes on the North Loup River bed were mapped using the orthorectified UAV photomosaic
233 that shows subaqueous bars and dunes, collected by Swanson et al. (2018). The orientation of
234 each dune was estimated by a best-fit line to a series of mapped brink points. The normal to
235 each brink line, in turn, was taken as the local transport direction for that dune, $\theta_{D-CHANNEL}$. θ_{D-}
236 *CHANNEL* was then tied to a point located at the average XY coordinate of all XY coordinates
237 defining that particular dune brink line. The same process was applied to bedforms over the 32
238 km reach of the Trinity River imaged using sonar profiles of dunes on the channel bed (dataset
239 from Mason, 2018), as well as dunes frozen on subaerially exposed point bar surfaces formed
240 during the previous bankfull flood imaged in a 2015 lidar survey (Mason and Mohrig, 2018;
241 2019b). The widths of these channels are comparable to the widths of the ridges, and the
242 braided and meandering end-members are useful in interpreting the Ruby Ranch Member, as
243 the dominance of free bars in the former vs. point bars in the latter route flow in different ways
244 (Dietrich & Smith, 1984; Ashworth, 1996). In the Ruby Ranch Member, values for $\theta_{D-RIDGE}$ are
245 taken from field measurements of planform trough cross strata across the top surfaces of the
246 two ridges and assigned associated XY coordinates at the center of the corresponding mapped
247 set.

248

249 **RESULTS**

250 **Vertical sections**

251 The vertical sections measured along the perimeters of each ridge were composed of
252 over 99% cross-stratified sandstones and conglomerates. The top surfaces of mudstones in the
253 vertical sections are scoured into by erosional surfaces that extend across ridges. Mudstone
254 units vary in thickness over short distances because they were eroded by overlying channel
255 elements, attaining a maximum thickness of 0.6 m. These persistent erosional surfaces
256 commonly define and separate individual channel-belts (Fig. 5A and B and 6A and B; Friend et
257 al., 1979). Any given vertical section exposes 1-4 stacked stories which locally vary in thickness
258 from 0.10 m to 8.60 m, with a mean of $3.10 \text{ m} \pm 0.22 \text{ m}$ (the calculated standard error of the
259 mean), median of $2.80 \text{ m} \pm 0.27 \text{ m}$ (the calculated standard error of the median) and σ of 2.03
260 $\text{m} \pm 0.15 \text{ m}$ (the calculated standard error of the standard deviation; $n = 89$; Fig. 6C). These
261 story-bounding surfaces are also exposed along the top surfaces of the ridges. Five of these
262 surfaces have been mapped across the western ridge, and four have been mapped across the
263 eastern ridge (Fig. 5C).

264

265 **Sedimentary structures and architecture**

266 The most common sedimentary structures preserved in planview and vertical exposures
267 of the Ruby Ranch Member ridges are trough cross sets (Fig. 7) with median grain sizes ranging
268 from upper-fine sand to medium pebbles (Fig. 8A to C). The mean thickness of these sets is 0.12
269 $\text{m} \pm 0.005 \text{ m}$, with a standard deviation of $0.09 \text{ m} \pm 0.003 \text{ m}$, and a coefficient of variation of
270 0.79 ± 0.04 ($c_v = \sigma/\text{mean}$, with propagated errors; $n = 350$). Along the top ridge surfaces where
271 these structures are exposed and mapped in planview (Fig. 9), the dominant dip direction of

272 these sets was identified as representative of the associated bedform's migration direction. The
273 polygons outlining these planform exposed sets ($n = 1,071$) sum to a total area of $5,019 \text{ m}^2$. Of
274 the 1,071 sets mapped in planform, 269 were identified as conglomerate, representing 25.1%
275 of sets and 26.5% ($1,330 \text{ m}^2$) of total set area. The remaining 802 sets were identified as
276 sandstone, representing 74.9% of sets and 73.5% ($3,689 \text{ m}^2$) of total set area. Larger scale
277 thicker compound cross-sets ($n = 12$), with a mean of $1.28 \text{ m} \pm 0.05 \text{ m}$ and a σ of $0.19 \text{ m} \pm 0.04$
278 m measured at preserved rollovers (topsets), are also exposed in planview (Fig. 10A-D). There
279 was no overlap in thickness between the two structures. The locations of planview
280 measurements of both types of sedimentary structures are shown in Figure 11. The summed
281 planform exposure area of these sets ($n = 103$) is 520 m^2 , or covering 10.3% of the planform
282 area of trough cross-sets. Within individual channel belt stories, shingled trough cross-sets
283 record transport up and down larger-scale topography (Fig. 12A-D).

284 Four arrangements of cross beds, types A, B, C, and D, were observed (Figs. 13-14).
285 Types A, B, and C appear in sandstones, and Type D appears only in pebble conglomerates.
286 Type A feature a thick basal set of compound strata scoured along its top by an upstream-
287 dipping surface, and overlain by a thinner coset composed of smaller cross beds with a mean
288 thickness and standard deviation of $0.12 \text{ m} \pm 0.01 \text{ m}$ and $0.07 \text{ m} \pm 0.01 \text{ m}$ (Fig. 13 and 14A-B).
289 The upstream dips of the scour surface range from 5° - 13° (mean = 7° , $n = 6$). In this case, the
290 orientation of small cross beds is roughly parallel the dip direction of the larger cross beds.

291 Type B feature a thick basal set of compound cross-sets that change both dip and
292 thickness in the downstream direction (Figs. 13 and 14C-D). Individual cross beds thicken by as

293 much as 300% over the course of 1.5 meters in the downstream direction (0.08 m to 0.23 m,
294 0.07 m to 0.23 m, and 0.06 m to 0.19 m). Correspondingly, the bounding surfaces separating
295 these cross beds shallow downstream from as steep as 26° to as shallow as 5°, and the upper
296 bounding surface transitions from being markedly erosional to conformable. Similar to type A,
297 the smaller cross beds roughly parallel the dip direction of the larger cross beds. The mean
298 thickness and standard deviation of these sets at shallowly dipping sections was 0.13 m ± 0.01
299 m, and 0.08 m ± 0.01 m.

300 Type C is also composed of compound strata, but in these cases the dip directions of the
301 smaller foresets were roughly transverse to the dip direction of the larger cross beds (Figs. 13
302 and 10D). Type C sets were mostly identified in plan-view exposures, so set thickness
303 measurements were not made.

304 Type D feature no compound cross-stratification, and bounding surfaces were sub-
305 horizontal or showed local variable curvature associated with trough geometry (Figs. 13 and
306 14E-F). Type D strata have a ~ 90° scatter of transport directions, apparent by the juxtaposition
307 of trough and dip-normal exposures (Slingerland and Williams, 1979). The mean thickness and σ
308 of type D sets was 0.19 m ± 0.02 m and 14.7 m ± 0.02 m, and sections contain up to ten stacked
309 sets.

310

311 **Transport anomalies**

312 Maps of transport anomalies (θ_{TA}) for the Ruby Ranch Member channel belts and North
313 Loup River are presented in Fig. 15A to C. The associated θ_{TA} histograms and statistical
314 moments for these systems and the Trinity River are presented in Figure 16A to D. All datasets
315 have mean values ranging between -12 and +6 degrees, and standard deviations ranging from
316 25° to 35°. In the North Loup River, anomalies were driven by flow routing around bars (Fig.
317 17B). Measurements approach the reach mean when assembled over a downstream distance
318 of ~3 bar lengths, or half the reach length, indicating adequate sampling (Figs. 15C and 17A to
319 C). In the Trinity River, as expected for meandering rivers, both the magnitude of the mean and
320 standard deviation of the transport anomalies are the smallest (Fig. 16D). Transport anomalies
321 that are observed are located along point bar surfaces (Dietrich and Smith, 1984). In the Ruby
322 Ranch Member, areas with concentrated high anomalies were found to be located at ridge
323 bends with concentrations of transport-normal-dipping accretion surfaces (Fig. 15A to B).

324

325 **DISCUSSION**

326 This discussion begins with interpretations of sedimentary structures deposited by the
327 ancient Ruby Ranch Member rivers. The avulsions, lateral migration, and aggradation of these
328 rivers (their kinematics) are then inferred through analysis of these sedimentary structures. A
329 regional depositional setting is then interpreted based on the kinematics of the rivers.

330 **Dune, bar, belt, and overbank strata**

331 A distinction is drawn between cross sets on either side of the break in scale shown in
332 Figure 8A. The thinner-bedded trough cross strata (Fig. 7) are interpreted as forming via the
333 migration of 3-D dunes with variably deep troughs (Rubin, 1987). In planform and vertical
334 sections, these are clearly distinct from larger-scale dipping strata (Fig. 10A to D), which do not
335 show the same bounding-surface curvature and, significantly, feature cross strata defined by
336 compound cross-sets (Figs. 10D and 14C to D). These larger-scale strata are interpreted as river-
337 bar sets (Edwards et al., 1983; Haszeldine, 1983; Almeida et al., 2016). The population of dip
338 direction vs. centerline trend anomalies for the bar strata feature a larger spread of values and
339 modes situated far from zero (compare Fig. 16A to D against Fig. 16E to F). The range of values,
340 particularly the prevalence of paleoflow-normal values, suggests the formative bar types
341 included point bars with primarily cross-stream accreting surfaces (Fig. 10D), and free bars
342 which can feature cross-stream-, downstream-, and upstream-dipping accretion surfaces
343 (Smith, 1972; Skelly et al., 2003; Almeida et al., 2016). Point bar structures are also interpreted
344 from ridge-scale observations, where clusters of bar surfaces dip towards the convex sides of
345 ridge bends (Fig. 11A to B; note that the western-most point bar strata define a convex-north
346 bend, Fig. 1C). Free bars, discussed below, can be observed on a much smaller scale, and are
347 represented by bar accretion surfaces not associated with a point bar (Fig. 11A to B).

348 Together, these dune- and bar-scale cross strata are interpreted as channel belts formed
349 during episodes of active sediment transport in channels ~1.28 m deep, based on bar thickness
350 (Mohrig et al., 2000). The mudstones associated with ridge-scale erosional surfaces are
351 interpreted to represent sedimentation during periods of channel abandonment, which
352 indicates a system that experienced multiple avulsions and channel reoccupations (Mohrig et

353 al., 2000; Jones and Hajek, 2007; Cuevas Martínez et al., 2010). The observed mudstone layers
354 are laterally discontinuous, which we interpret as due to local scour associated with re-
355 occupation that created the erosional surface. Thus, the ridges represent channel-belt
356 complexes composed of stacked, individual channel belts, and the stratigraphic continuity
357 between the two ridges suggests they once formed a continuous deposit.

358 The four cross-stratal types A through D observed in the Ruby Ranch Member ridges
359 document the interaction of the ancient dunes and bars in the formative river channels (Figs. 13
360 and 14). Type A architectures are characteristic of free bars, and possess a bar-scale bounding
361 surface separating bar lee strata below from deposits of the bar-stoss surface above (Fig. 14A to
362 B). As such, this bounding surface preserves the characteristic dip of the stoss side of the bar
363 form. The bar-lee strata may be compound in that they are composed of dune cross sets, or bar
364 slip faces, which may nonetheless be influenced by superimposed dunes and ripples (Reesink
365 and Bridge, 2011; Reesink, 2018). Theory (Paola and Borgman, 1991) and a recent
366 morphodynamic bedform model (Swanson et al., 2019) show that set stacking can occur even
367 under conditions of net bypass or erosion because of variability in dune scour depths.

368 Type B architectures highlight change in compound dune strata due to migration of free
369 bars (Figs. 13 and 14C to D). The steepest 26° cross strata represent bar-lee construction most
370 perpendicular to the average transport direction observed. The observed shallowing of
371 bounding-surface dips and thickening of sets in the downstream direction records the planform
372 deformation of the bar crest over time, where steep downstream-accreting surfaces gradually
373 become more laterally accreting. As evident from the compound nature of these sets, this bar

374 growth is driven by dune accretion in front of the bar. At the two locations where A and B type
375 architectures are adjacent (Figs. 14A to D), the transition of the stoss scour surface to the
376 conformable bounding surface of a bar cross-stratum represents the delivery of sediment
377 mined from the bar stoss up and over the crest of the bar, and onto the bar lee. Taken
378 together, these two architectures preserve the processes associated with bar migration via the
379 mining and delivery of sediment by a surface veneer of smaller dunes compound to a larger
380 free bar. One lateral section shows the stacking of stoss strata on lee strata, recording the
381 aggradation and migration of a bar (Fig. 14G to H).

382 The type C compound strata define bar growth at an oblique angle to the net transport
383 direction, and define the lateral migration of a bank-attached bar form (Fig. 10D). The coarser,
384 non-compound type D architectures are interpreted as thalweg deposits (Fig. 14E to F).
385 Together, these four architectural types describe the construction of channel-bottom
386 topography within individual channel belts via the migration and growth of dunes (both on bars
387 and in the thalweg), free bars, and point bars.

388

389 **Channel-bed topography**

390 Preserved bar form topography is interpreted to record the moment of channel
391 abandonment (Fig. 12A to D). Two lines of evidence support this. First, in both cross section and
392 map view, the compound relationship between dune and bar strata informs us that entire bar
393 forms are preserved, complete with bar rollovers that represent the tops of bars (topset, Figs.
394 12, 13, 14, and 19). Second, the stoss-positioned dune sets are restricted to a surface veneer

395 composing less than the upper 25% of the bar, with the remainder composed of steeply dipping
396 bar-scale strata. If erosion of ridge surfaces commonly broke through the surface veneer of
397 stoss dune sets, then large bar scale strata would constitute a greater percentage of
398 sedimentary structures exposed on ridge surfaces. Given that sandstone trough cross sets,
399 which are interpreted as superimposed on bars, constitute nearly 75% of all mapped sets, we
400 would interpret a less well-preserved channel bed to expose up to 75% bar strata. Instead,
401 dunes occupy an order of magnitude more surface area of the outcrop. The preservation of the
402 river-bottom topography at the time of avulsion is interpreted to be the consequence of a
403 relatively rapid channel abandonment coupled with minimal erosion of the channel belt by the
404 subsequent channel reoccupation.

405

406 **Channel-planform geometry**

407 The near zero means and the high kurtosis of the Ruby Ranch Member Formation
408 paleotransport anomaly measurements, coupled with the similarity of the standard deviations
409 measured in the ancient and the modern, are interpreted to indicate that the channel-belt-
410 complex geometry preserves the formative river centerline in a reliable way (Fig. 16A to D).
411 Regions of the channel belts showing concentrations of high transport anomaly measurements
412 are associated with point bar lateral accretion surfaces (Figs. 1C, 11A to B, and 16A to B),
413 supporting the hypothesis that lateral point bar migration is a cause of high anomaly
414 measurements (Fig. 4B). However, these regions do not represent a majority of the ridge area.

415 The studied ridges are composed of several vertically stacked channel belts. The
416 preservation of the formative river channel centerlines through multiple re-occupations of the
417 channel is expected in fluvial settings with high rates of vertical aggradation within the channel
418 relative to lateral migration rates (Gibling, 2006; Jerolmack and Mohrig, 2007). As a result,
419 there is a general lack of centerline distortion, even though the ridge represents a complex of
420 stacked channel belts.

421

422 **Channel-belt thickness**

423 Because avulsions are likely to occur when a channel bed has aggraded to a sufficient
424 level of superelevation, the thickness of a preserved channel belt, on average, is posited to
425 equal paleochannel depth plus an aggradational component. The thickness of a fine bar sets
426 from topset to bottomset is assumed to be a measure of local channel depth (Mohrig et al.,
427 2000). Bar measurements reported in Fig. 8A suggest an overall, mean channel depth of $1.28 \pm$
428 0.05 m. The mean belt thickness of $3.10 \text{ m} \pm 0.22 \text{ m}$ (Fig. 6C) is then composed of an
429 aggradational component consisting of $1.82 \text{ m} \pm 0.20 \text{ m}$. This indicates that, on average, a
430 channel belt accumulated a thickness of 1.53 ± 0.22 times its original depth before avulsing,
431 creating a channel belt with a total thickness of 2.42 ± 0.19 times its flow depth.

432

433 **River-bed kinematics**

434 *Dune accumulation on bars and in the thalweg*

435 Analysis of Paola and Borgman (1991) shows that bedforms with gamma-distributed
436 heights create a predictable exponential distribution of set thicknesses in cases of no net
437 aggradation. Bridge and Best (1997) and Jerolmack and Mohrig (2005) emphasize the
438 importance of bed aggradation as a control on the distribution of set thickness, showing that
439 increased aggradation rates decrease the relative control of variable scour depth on set
440 thickness. Jerolmack and Mohrig (2005) showed that the coefficient of variation (c_v) of set
441 thicknesses decreases from a value of 0.88 in the case of no aggradation, to values approaching
442 the c_v of the formative bedform heights with significant bed aggradation. Coupled with this
443 change in c_v is a gradual shift from the predicted exponential distribution of set thicknesses, to
444 a gamma distribution mirroring the distribution of the formative bedforms. Significantly, this
445 analysis has been shown to be general enough to apply to ancient fluvial (Jerolmack and
446 Mohrig, 2005) and aeolian strata (Swanson et al., 2019; Cardenas et al., 2019). Therefore, the
447 reporting and analysis of set thickness distributions should be considered a significant part of
448 any quantitative reconstruction of clastic sedimentary systems where there is an interest in
449 understanding the kinematics and transport within the ancient system.

450 When taken together, all measured dune set thicknesses ($n = 350$) have a c_v of $0.79 \pm$
451 0.04 (Fig. 8A). This value implies set production by variable scour under conditions of minimal
452 bed aggradation ($c_v = 0.88 \pm 0.03$ for bypass case in Bridge 1997). The scour-dominated case
453 also creates laterally discontinuous sets (Jerolmack and Mohrig, 2005; Cardenas et al., 2019).
454 This scour dominance appears to be at odds with the well-preserved bars described above (Figs.
455 14C to D). To understand the construction of the channel belt, measurements must be locally
456 standardized to account for variability in bedform height at the reach scale, which is not

457 necessarily representative of local variability (Reesink et al., 2015). Assembling all
458 measurements into a single calculation without considering local architecture can result in
459 inaccurate interpretations.

460 Set-thickness analysis performed separately for bar-lee sets, bar-stoss sets, and thalweg
461 sets yields a different result than the bulk description. The first step in analyzing data from each
462 sub-environment was to divide each set thickness by the mean set thickness for its local coset.
463 These dimensionless values of set thickness were then collected for every bar-lee, bar-stoss,
464 and thalweg deposit. Standardized cumulative distribution functions (CDFs) are shown in Figure
465 18. Coefficients of variation for the standardized distributions are 0.29 ± 0.04 for lee sets, $0.47 \pm$
466 0.07 for stoss sets, and 0.67 ± 0.10 for thalweg sets. Although c_v values as low as 0.29 were not
467 examined by Jerolmack and Mohrig (2005), interpolation of their Figure 4B leads to a ratio of
468 aggradation rate (r) to migration rate (c) for lee sets of $\sim 10^{-1}$ (climb angle from 5° - 6°). Stoss sets
469 have r/c of $\sim 10^{-1.5}$ (climb angle from 1° - 2°), and thalweg sets have r/c of $\sim 10^{-2.5}$ (climb angle
470 from 0.1° - 0.2°). The lee sides of downstream-migrating barforms, where the most sediment
471 accumulation is expected (Reesink et al., 2015), have the highest ratio of aggradation rate to
472 migration rate. This significant aggradation is supported by a Kolmogorov-Smirnov statistical
473 test comparing the measurements to fitted exponential and gamma curves (Fig. 18A to C). For
474 lee sets, the exponential curve is rejected at a significance level of 0.05 ($p < 0.001$), and the
475 gamma curve is not ($p = 0.46$). This is consistent with the observed stacking and downstream
476 thickening of sets in lee-type architectures (Fig. 14C to D). Even though thalweg sets are
477 rejected as being exponentially distributed ($p = 0.02$) and not rejected as gamma distributed (p
478 $= 0.17$), the two fitted curves are more similar than in the lee and stoss cases.

479 A non-trivial amount of climb is recorded by stoss sets, given the c_v of 0.47 ± 0.07 ,
480 rejection of an exponential fit ($p = 0.01$), and non-rejection of a gamma fit ($p = 0.90$). This
481 indicates some degree of upstream accumulation driven by the stoss-side aggradation of dune
482 sets, likely during the final flood (Lunt and Bridge, 2004). Using ground-penetrating radar cross
483 sections, Skelly et al. (2003) also interpreted upstream accretion in modern bars of the Niobrara
484 River, Nebraska, USA, which represent the growth and deformation of bars as they migrate.

485

486 *Constraints on the time recorded by individual channel belts*

487 How is time distributed through Ruby Ranch Member channel belts? Backing out
488 sedimentation rates from these strata would provide information on the kinematics of the
489 formative rivers, as well as how local controls might dictate the construction of the rock record
490 (Sadler, 1981; Jerolmack and Sadler, 2015; Paola et al., 2018). The distribution of cross-set
491 thicknesses, in conjunction with assumed bedform migration rates, can provide some sense of
492 the minimum amount of time associated with aggradation of each channel belt. This analysis is
493 performed for the two major channel belt components observed here, bar and thalweg
494 accumulations.

495 Given that the accumulation of dune sets at the bar lee is the process through which
496 these bars migrated (Fig. 14C to D), it follows that

$$497 \quad r_{lee} / c_{lee} = s_{bar} / m_{bar} \quad (2)$$

498 where r_{lee} is the aggradation rate of the bed, c_{lee} is the migration rate of dunes, r_{lee} / c_{lee} of bar
499 lee sets is calculated in the prior section as 10^{-1} , and s_{bar} / m_{bar} is the bar thickness over the
500 equivalent migration distance (Fig. 19). Solving for m_{bar} , the only unknown, yields $12.8 \text{ m} \pm 0.5$
501 m of bar migration, with uncertainty based on the number of measurements. Downstream-
502 migrating bars migrate ~ 10 m per day in the North Loup and other rivers (Meade, 1985; Mohrig
503 and Smith, 1996). Assuming 10 m per day is a comparable rate to the ancient Ruby Ranch
504 Member fluvial system, which is a reasonable, order of magnitude assumption given the similar
505 flow depths, channel widths, and the distribution of dune heights in the North Loup relative to
506 our measured cross-set thicknesses (Mohrig and Smith, 1996), the observed lee architectures
507 are a record of only $\sim 1.28 \pm 0.05$ days of sedimentation. This suggests the bar strata and
508 associated compound dune strata do not record the gradual aggradation of the channel bed
509 leading up to avulsion, but rather record the higher frequency modification of the channel bed
510 via bar migration. Instead, it is hypothesized that the aggradation of the channel bed is
511 recorded in thalweg strata. To test this hypothesis, Equation 2 is redefined in terms of the
512 thalweg sets and the average thickness of the aggradational component of the channel belts,
513 with a slower aggradation rate predicted. Assuming steady construction at North Loup dune
514 migration rates (~ 60 m per day, Mohrig and Smith, 1996), only $9.7 \text{ days} \pm 1.1 \text{ days}$ are required
515 to accumulate the thalweg strata reported here. While indeed longer-term accumulations than
516 the bar strata, these sets do not record slow channel aggradation over avulsion timescales.

517 For most rivers, occupation may last anywhere from years to thousands of years
518 (Stouthamer and Berendsen, 2001; Slingerland and Smith, 2004). It is unlikely these channels
519 were only occupied for 9.7 days. Instead, these strata may only represent the aggradation and

520 scour filling that occurred during the final episode of sedimentation that preceded avulsion and
521 channel abandonment. This episode is likely to coincide with the final flood prior to avulsion.
522 This result suggests that the channel was in a state of net bypass for most of its occupation, or
523 close enough to it that subsequent scouring during floods removed any slowly accumulated
524 strata. Had channel abandonment not prevented it, the flood-associated aggradation recorded
525 by each channel belt would likely have been reworked to a lower, possibly pre-flood elevation
526 (Fig. 20). The complete reworking of the channel bed during flood stage has been observed in
527 modern net-depositional rivers (Nittrouer et al., 2011a) and in experiments (Leary and Ganti,
528 2020). This also suggests that floodplain deposits might more completely record successive
529 episodes of flood-stage deposition than channel belts, as presumably an episode of floodplain
530 deposition is not immediately followed by reworking.

531

532 **Channel vs. floodplain accumulation**

533 On average, a formative river of the Ruby Ranch Member constructed a channel belt
534 that was 2.42 ± 0.19 times thicker than its characteristic flow depth before avulsing. This
535 thickness to depth ratio is somewhat larger than the value of 1.84 measured for the ancient
536 Guadalupe-Matarranya fluvial system in Spain (Mohrig et al., 2000; their Table 2). Without
537 preserved levee deposits, it is unclear whether the increased relative belt thickness recorded by
538 the Ruby Ranch Member is connected to an increase in incision depth or channel
539 superelevation. However, the preservation of mudstones between vertically stacked channel
540 belts, as well as preserved bar rollovers suggest that the standardized incision depths for the

541 Ruby Ranch Member were comparable to the Guadalupe-Matarranya system (Mohrig et al.,
542 2000). Assuming that the threshold superelevation trigger for avulsion proposed by Mohrig et
543 al. (2000) is suitably general, the increased bed aggradation for Ruby Ranch channel belts is
544 hypothesized to have required increased Ruby Ridge floodplain aggradation compared to the
545 Guadalupe-Matarranya system. That is, in order for the channel bed to reach the threshold
546 superelevation to avulse, more channel bed aggradation was required during the final
547 depositional episode to catch up with levees and floodplain that steadily aggraded during each
548 bankfull event (Fig. 20). This scenario is consistent with the interpreted reworking of the
549 channel bed between bankfull events, where any associated accumulation and scouring are
550 reworked or filled such that there is not enough net channel bed change to avoid scouring by
551 the following flood. This is contrasted by steady, gradual levee and floodplain aggradation,
552 assuming these overbank environments are less likely to be reworked between floods.

553

554 **Large-scale depositional setting**

555 The interpreted kinematics of the Ruby Ranch Member rivers are consistent with the
556 kinematics reported for megafan channels. Channels in Andean megafans are highly unstable
557 and mobile, and avulse on the scale of years, limiting any significant lateral migration (e.g.,
558 Horton and DeCelles, 2001; Chakraborty et al., 2010). Broader channel belts can develop on
559 megafans, but these are generally limited to meandering rivers confined within lobe-cutting
560 incised valleys that prevent avulsions (Assine et al., 2014). We therefore interpret the Ruby
561 Ranch Member of the Cedar Mountain Formation to represent the accumulations of an early

562 Cretaceous megafan or megafans draining the Sevier orogenic belt. Given the importance of
563 floodplain aggradation in stacking these channel belts, the Ruby Ranch Member likely
564 represents a medial fan setting (Owen et al., 2015). This contribution is useful in that a regional
565 interpretation of depositional setting can be made using only local sedimentology, possibly
566 even in cores, without the dependence on observing fan-scale changes in facies which may not
567 be exposed well enough in all formations (e.g., Owen et al., 2015).

568

569 **CONCLUSIONS**

570 Remnant, erosion-resistant ridges of the Ruby Ranch Member of the Cretaceous Cedar
571 Mountain Formation are channel-belt complexes, composed of five or six stacked channel belts.
572 Each channel belt is composed of bar and dune strata that exhibit a variety of compound
573 relationships indicating the role of the latter in the accumulation of the former. In simple terms,
574 bars created topography, which forced dune sedimentation in the space in front of or next to a
575 bar, which then drove further bar migration.

576 Free-bar migration rates are estimated from thickness distributions of compound dune
577 cross strata. Free bars represent only about 1 day of accumulation, yet they comprise on
578 average 41% of a channel belt's total thickness. Accumulations of dunes in the thalweg
579 represent the rest of the belt and the aggradation of the channel bed, and are distinct from bar
580 strata. Thalweg cross-set-thickness distributions are used to estimate the duration of bed
581 aggradation at only about 10 days. These 10 days are interpreted to represent the final bankfull
582 episode preceding avulsion, rather than the duration of the entire occupation of the channel.

583 Prior bankfull accumulations that did not lead to avulsion were reworked to lower elevations by
584 subsequent non-flood flows. Therefore, these channels primarily functioned as conduits for
585 bypassing sediment, and most of the total time recorded by these channel belts is represented
586 by their basal erosional surfaces.

587 Two aspects of the formative river systems are preserved particularly well, and record
588 frequent and rapid avulsions, and a minor amount of total lateral migration. First, free bars are
589 preserved completely, from stoss to lee, and are observed in both vertical sections and as
590 topography on ridge tops. This observation is significant on its own; if this paleobar topography
591 can be detected using remote sensing, future analysis could use it to better constrain flow
592 depths of ancient rivers from fluvial channel belts exposed at the surface of Mars. Second, the
593 planform geometry of the ridge and channel-belt complex represents the planform geometry of
594 the formative rivers well, despite multiple reoccupations. Frequent, rapid avulsions and limited
595 lateral migration are consistent with megafan channels, thus we interpret a megafan as the
596 depositional setting of these channel-belt complexes. This provides a way to interpret regional
597 depositional setting using the local sedimentology, rather than requiring regional exposure
598 showing predicted facies changes.

599 Significantly, this synthesis of vertical and planform channel belts measurements
600 provides a baseline for future studies facilitated by high resolution, drone-derived planform
601 datasets. The workflow presented here may be particularly useful for the upcoming 2020 Mars
602 Rover mission to Jezero crater, Perseverance, which will examine exhumed fluvial and deltaic
603 strata using rover-mounted cameras and the first helicopter drone on Mars, Ingenuity.

604

605 **ACKNOWLEDGEMENTS**

606 We thank Chief Editor Ian Kane, Associate Editor Christopher Fielding, Arjan Reesink,
607 Matt Joeckel, and two anonymous reviewers for constructive feedback that helped improve this
608 manuscript. Hima Hassenruck-Gudipati, Woong Mo Koo, and David Brown are thanked for their
609 field assistance. The staff of Green River State Park, Utah, were accommodating to our large
610 group. This paper has improved following discussions with members of the David Mohrig
611 Research Group and the Quantitative Clastics Laboratory, as well as Wonsuck Kim, Joel Johnson,
612 Zoltan Sylvester, Cole Speed, Paola Passalacqua, Alistair Hayden, Mike Lamb, Becky Williams,
613 Jenn Pickering, and Tim Demko. Funding was provided by the University of Texas Jackson
614 School of Geosciences, the University of Texas Graduate School, and the RioMAR Industry
615 Consortium.

616

617 **DATA AVAILABILITY**

618 The data that support the findings of this study are available from the corresponding
619 author upon reasonable request.

620

621 **REFERENCES**

- 622 **Allen, J.R.L.** (1970) A Quantitative Model of Climbing Ripples and Their Cross-Laminated
623 Deposits. *Sedimentology*, **14**, 5–26.
- 624 **Allen, J.R.L.** (1983) Studies in fluvial sedimentation: bars, bar-complexes and sandstone
625 sheets (low-sinuosity braided streams) in the Brownstones (L. Devonian), Welsh
626 Borders. *Sedimentary Geology*, **33**, 237–293.
- 627 **Almeida, R.P., Freitas, B.T., Turra, B.B., Figueiredo, F.T., Marconato, A., and Janikian, L.** (2016)
628 Reconstructing fluvial bar surfaces from compound cross-strata and the interpretation
629 of bar accretion direction in large river deposits. *Sedimentology*, **63**, 609–628.
- 630 **Ashworth, P.J.** (1996) Mid-channel bar growth and its relationship to local flow strength and
631 direction. *Earth Surface Processes and Landforms*, **21**, 103-123.
- 632 **Assine, M.L., Corradini, F.B., Pupim, F. do N., and McGlue, M.M.** (2014) Channel arrangements
633 and depositional styles in the São Lourenço fluvial megafan, Brazilian Pantanal wetland.
634 *Sedimentary Geology*, **301**, 172-184.
- 635 **Berens, P.** (2009) CircStat: A MATLAB Toolbox for Circular Statistics. *Journal of Statistical*
636 *Software*, **31**, 1-21.
- 637 **Bridge, J.S.** (1997) Thickness of sets of cross strata and planar strata as a function of formative
638 bed-wave geometry and migration, and aggradation rate. *Geology*, **25**, 971-974.

639 **Bridge, J.S., and Best, J. (1997)** Preservation of planar laminae due to migration of low-relief
640 bed waves over aggrading upper-stage plane beds: comparison of experimental data
641 with theory. *Sedimentology*, **44**, 253-262.

642 **Burr, D.M., Enga, M.-T., Williams, R.M., Zimbelman, J.R., Howard, A.D., and Brennand, T.A.**
643 (2009) Pervasive aqueous paleoflow features in the Aeolis/Zephyria Plana region, Mars.
644 *Icarus*, **200**, 52-76.

645 **Cardenas, B.T., Mohrig, D., and Goudge, T.A. (2018)** Fluvial stratigraphy of valley fills at Aeolis
646 Dorsa, Mars: Evidence for base-level fluctuations controlled by a downstream water
647 body. *Geological Society of America Bulletin*, **130**, 484-498.

648 **Cardenas, B.T., Kocurek, G., Mohrig, D., Swanson, T., Hughes, C.M., and Brothers, S.C. (2019)**
649 Preservation of autogenic processes and allogenic forcings within set-scale aeolian
650 architecture II: the scour-and-fill dominated Jurassic Page Sandstone, Arizona, USA.
651 *Journal of Sedimentary Research*, **89**, 741-760.

652 **Cardenas, B.T., Swartz, J.M., Mohrig, D., Prokocki, E.W.** Setting up the preservation of fluvial
653 channel belts. Preprint available at EarthArxiv. DOI: 10.31223/osf.io/y7m4w

654 **Carling, P.A., and Leclair, S.F. (2019)** Alluvial stratification styles in a large, flash-flood
655 influenced dryland river: The Luni River, Thar Desert, north-west India. *Sedimentology*,
656 **66**, 102-128.

657 **Carpenter, K. (2014)** Where the sea meets the land: the unresolved Dakota problem in Utah.
658 *Utah Geological Association Publication*, **43**, 357-372.

659 **Chadwick, A.J.** (2020) Mechanics of river avulsions on lowland river deltas. *PhD Dissertation,*
660 *California Institute of Technology*, <https://doi.org/10.1029/2019GL082491>.

661 **Chakraborty, T., Kar, R., Ghosh, P., and Basu, S.** (2010) Kosi megafan: Historical records,
662 geomorphology and the recent avulsion of the Kosi River. *Quaternary International*, **227**,
663 143-160.

664 **Chamberlin, E.P., and Hajek, E.A.** (2015) Interpreting paleo-avulsion dynamics from multistory
665 sand bodies. *Journal of Sedimentary Research*, **85**, 82–94.

666 **Chamberlin, E.P., and Hajek, E.A.** (2019) Using bar preservation to constrain reworking in
667 channel-dominated fluvial stratigraphy. *Geology*, **47**, 531-534.

668 **Cuevas Martínez, J.L., Cabrera Pérez, L., Marcuello, A., Arbués Cazo, P., Marzo Carpio, M., and**
669 **Bellmunt, F.** (2010) Exhumed channel sandstone networks within fluvial fan deposits
670 from the Oligo-Miocene Caspe Formation, South-east Ebro Basin (North-east Spain).
671 *Sedimentology*, **57**, 162–189.

672 **Currie, B.S.** (1998) Upper Jurassic-Lower Cretaceous Morrison and Cedar Mountain Formations,
673 Ne Utah-NW Colorado: Relationships between Nonmarine Deposition and Early
674 Cordilleran Foreland-Basin Development. *Journal of Sedimentary Research*, **68**, 632-652.

675 **Currie, B.S.** (2002) Structural configuration of the Early Cretaceous cordilleran foreland-basin
676 system and the Sevier thrust belt, Utah and Colorado. *The Journal of Geology*, **110**, 697-
677 718.

678 **Davis, J.M., Balme, M., Grindrod, P.M., Williams, R.M.E., and Gupta, S.** (2016) Extensive
679 Noachian fluvial systems in Arabia Terra: implications for early Martian climate.
680 *Geology*, **44**, 847-850.

681 **DeCelles, P.G., Langford, R.P., and Schwartz, R.K.** (1983) Two New Methods of Paleocurrent
682 Determination from Trough Cross-Stratification. *Journal of Sedimentary Research*, **53**,
683 629-642.

684 **Dietrich, W.E., and Smith, J.D.** (1984) Bed load transport in a river meander. *Water Resources*
685 *Research*, **20**, 1355-1380.

686 **Dott, R.H., Jr.** (1973) Paleocurrent Analysis of Trough Cross Stratification. *Journal of*
687 *Sedimentary Research*, **43**, 779-783.

688 **Durkin, P.R., Hubbard, S.M., Holbrook, J., and Boyd, R.** (2018) Evolution of fluvial meander-belt
689 deposits and implications for the completeness of the stratigraphic record. *Geological*
690 *Society of America Bulletin*, **130**, 721-739.

691 **Edmonds, D.A., Hajek, E.A., Downton, N., and Bryk, A.B.** (2016) Avulsion flow-path selection on
692 rivers in foreland basins. *Geology*, **44**, 695–698.

693 **Edwards, M.B., Eriksson, K.A., and Kier, R.S.** (1983) Paleochannel geometry and flow patterns
694 determined from exhumed Permian point bars in north-central Texas. *Journal of*
695 *Sedimentary Research*, **53**, 1261-1270.

696 **Friend, P.F., Slater, M.J., and Williams, R.C.** (1979) Vertical and lateral building of river
697 sandstone bodies, Ebro Basin, Spain. *Journal of the Geological Society*, **136**, 39–46.

698 **Ganti, V., Paola, C., and Fofoula-Georgiou, E.** (2013) Kinematic controls on the geometry of
699 the preserved cross sets. *Journal of Geophysical Research: Earth Surface*, **118**, 1296-
700 1307.

701 **Garrison, J.R., Brinkman, D., Nichols, D.J., Layer, P., Burge, D., and Thayn, D.** (2007) A
702 multidisciplinary study of the Lower Cretaceous Cedar Mountain Formation,
703 Mussentuchit Wash, Utah: a determination of the paleoenvironment and paleoecology
704 of the *Eolambia caroljonesa* dinosaur quarry. *Cretaceous Research*, **28**, 461–494.

705 **Gibling, M.R.** (2006) Width and thickness of fluvial channel bodies and valley fills in the
706 geological record: a literature compilation and classification. *Journal of Sedimentary*
707 *Research*, **76**, 731–770.

708 **Goudge, T.A., Mohrig, D., Cardenas, B.T., Hughes, C.M., and Fassett, C.I.** (2018) Stratigraphy
709 and paleohydrology of delta channel deposits, Jezero crater, Mars. *Icarus*, **301**, 58–75.

710 **Hajek, E.A., and Edmonds, D.A.** (2014) Is river avulsion style controlled by floodplain
711 morphodynamics? *Geology*, **42**, 199-202.

712 **Hartley, A.J., Owen, A., Swan, A., Weissmann, G.S., Holzweber, B.I., Howell, J., Nichols, G.,**
713 **and Scuderi, L.** (2015) Recognition and importance of amalgamated sandy meander
714 belts in the continental record. *Geology*, **43**, 679-682.

715 **Haszeldine, R.S.** (1983) Fluvial bars reconstructed from a deep, straight channel, Upper
716 Carboniferous coalfield of Northeast England. *Journal of Sedimentary Research*, **53**,
717 1233-1247.

718 **Hayden, A.T., Lamb, M.P., Fischer, W.W., Ewing, R.C., McElroy, B.J., and Williams, R.M.E.**
719 (2019) Formation of sinuous ridges by inversion of river-channel belts in Utah, USA, with
720 implications for Mars. *Icarus*, **332**, 91-110.

721 **Heller, P.L., and Paola, C.** (1989) The paradox of Lower Cretaceous gravels and the initiation of
722 thrusting in the Sevier orogenic belt, United States Western Interior. *Geological Society*
723 *of America Bulletin*, **101**, 864-875.

724 **Heller, P.L., and Paola, C.** (1996) Downstream changes in alluvial architecture: an exploration of
725 controls on channel-stacking patterns. *Journal of Sedimentary Research*, **66**, 297-306.

726 **Hooke, J.M., and Yorke, L.** (2011) Channel bar dynamics on multi-decadal timescales in an
727 active meandering bar. *Earth Surface Processes and Landforms*, **36**, 1910-1928.

728 **Hughes, C.M., Cardenas, B.T., Goudge, T.A., and Mohrig, D.** (2019) Deltaic deposits indicative
729 of a paleo-coastline at Aeolis Dorsa, Mars. *Icarus*, **317**, 442-453.

730 **Ikeda, H.** (1989) Sedimentary controls on channel migration and origin of point bars in sand-
731 bedded meandering rivers. In S. Ikeda and G. Parker (Eds.), *River Meandering: Water*
732 *Resources Monograph*, **12**, 51-68. American Geophysical Union: Washington, D.C.

733 **Ikeda, S., Parker, G., and Sawai, K.** (1981) Bend theory of river meanders. Part 1. Linear
734 development. *Journal of Fluid Mechanics*, **112**, 363-377.

735 **Jerolmack, D.J., and Mohrig, D.** (2005) Frozen dynamics of migrating bedforms. *Geology*, **33**,
736 57-60.

737 **Jerolmack, D.J., and Mohrig, D.** (2007) Conditions for branching in depositional rivers. *Geology*,
738 **35**, 463–466.

739 **Joeckel, R.M., Ludvigson, G.A., and Kirkland, J.I.** (2017) Lower Cretaceous paleo-Vertisols and
740 sedimentary interrelationships in stacked alluvial sequences, Utah, USA. *Sedimentary*
741 *Geology*, **361**, 1-24.

742 **Joeckel, R.M., Ludvigson, G.A., Möller, A., Hotton, C.L., Suarez, M.B., Suarez, C.A., Sames, B.,**
743 **Kirkland, J.I., and Hendrix, B.** (2019) Chronostratigraphy and terrestrial
744 palaeoclimatology of Berriasian-Hauterivian strata of the Cedar Mountain Formation,
745 Utah, USA. *Geological Society, London, Special Publications*, **498**,

746 **Jones, H.L., and Hajek, E.A.** (2007) Characterizing avulsion stratigraphy in ancient alluvial
747 deposits. *Sedimentary Geology*, **202**, 124-137.

748 **Kirkland, J.I., Cifelli, R.L., Britt, B.R., Burge, D.L., DeCourten, F.L., Eaton, J.G., and Parrish, J.M.,**
749 (1999) Distribution of vertebrate faunas in the Cedar Mountain Formation, east central
750 Utah, in Gillette, D.D., ed., *Vertebrate Paleontology in Utah: Utah Geological Survey*
751 *Miscellaneous Publication*, **1999–1**, 201–217.

752 **Kowallis, B.J., Heaton, J.S., and Bringham, K.** (1986) Fission-track dating of volcanically derived
753 sedimentary rocks. *Geology*, **14**, 19-22.

754 **Lazarus, E.D., and Constantine, J.A.** (2013) Generic theory for channel sinuosity. *Proceedings of*
755 *the National Academy of Sciences*, **110**, 8447-8452.

756 **Leary, K.C.P., and Ganti, V.** (2020) Preserved fluvial cross strata record bedform disequilibrium
757 dynamics. *Geophysical Research Letters*, **47**, <https://doi.org/10.1029/2019GL085910>.

758 **Ludvigson, G.A., Joeckel, R.M., González, L.A., Gulbranson, E.L., Rasbury, E.T., Hunt, G.J.,**
759 **Kirkland, J.I., and Madsen, S.** (2015) Correlation of Aptian-Albian carbon isotope
760 excursions in continental strata of the Cretaceous foreland basin, Eastern Utah, U.S.A.
761 *Journal of Sedimentary Research*, **80**, p. 955-974.

762 **Ludvigson, G.A., Joeckel, R.M., Murphy, L.R., Stockli, D.F., González, L.A., Suarez, C.A.,**
763 **Kirkland, J.I., and Al-Suwaidi, A.** (2015) The emerging terrestrial record of Aptian-Albian
764 global change. *Cretaceous Research*, **56**, 1-24.

765 **Lunt, I.A., and Bridge, J.S.** (2004) Evolution and deposits of a gravelly braid bar, Sagavanirktok
766 River, Alaska. *Sedimentology*, **51**, 415-432.

767 **Mahon, R.C., and McElroy, B.** (2018) Indirect estimation of bedload flux from modern sand-bed
768 rivers and ancient fluvial strata. *Geology*, **46**, 579-582.

769 **Maizels, J.K.** (1987) Plio-Pleistocene raised channel systems of the western Sharqiya (Wahiba),
770 Oman. *Geological Society of London, Special Publications*, **35**, 31–50.

771 **Maizels, J.** (1990) Raised channel systems as indicators of palaeohydrologic change: a case
772 study from Oman. *Palaeogeography, Palaeoclimatology, Palaeoecology*, **76**, 241–277.

773 **Maizels, J., and McBean, C.** (1990) Cenozoic alluvial fan systems of interior Oman:
774 palaeoenvironmental reconstruction based on discrimination of palaeochannels using
775 remotely sensed data. *Geological Society of London, Special Publications*, **49**, 565–582.

776 **Mason, J., and Mohrig, D.** (2018) Using time-lapse lidar to quantify river bend evolution on the
777 meandering coastal Trinity River, Texas, USA. *Journal of Geophysical Research: Earth*
778 *Surface*, **123**, 1133-1144.

779 **Mason, J., and Mohrig, D.** (2019a) Scroll bars are inner bank levees along meandering river
780 bends. *Earth Surface Processes and Landforms*, **44**, 2649-2659.

781 **Mason, J., and Mohrig, D.** (2019b) Differential bank migration and the maintenance of channel
782 width in meandering river bends. *Geology*, **47**, 1136-1140.

783 **Mason, J.** (2018) Sediment transport and the geomorphic evolution of the coastal Trinity River,
784 TX. *PhD Dissertation, University of Texas at Austin*, 167 p.

785 **McKee, E.D., and Weir, G.W.** (1953) Terminology for stratification and cross-stratification in
786 sedimentary rocks. *Geological Society of America Bulletin*, **64**, 381–390.

787 **Meade, R.H.** (1985) Wavelike movement of bedload sediment, East Fork River, Wyoming.
788 *Environmental Geology and Water Sciences*, **7**, 215-225.

789 **Miall, A.D.** (1977) A review of the braided-river depositional environment. *Earth-Science*
790 *Reviews*, **13**, 1-62.

791 **Miall, A.D.** (1985) Architectural-element analysis: a new method of facies analysis applied to
792 fluvial deposits. *SEPM Special Publication-Recognition of Fluvial Depositional Systems*
793 *and Their Resource Potential*, **19**, 33-81.

794 **Miall, A.D.** (1988) Architectural elements and bounding surfaces in fluvial deposits: anatomy of
795 the Kayenta formation (lower Jurassic), Southwest Colorado. *Sedimentary Geology*, **55**,
796 233–262.

797 **Miall, A.D.** (2015) Updating uniformitarianism: stratigraphy as just a set of ‘frozen accidents’.
798 *Geological Society of London, Special Publications*, **404**, 11-36.

799 **Mohrig, D., Heller, P.L., Paola, C., and Lyons, W.J.** (2000) Interpreting avulsion process from
800 ancient alluvial sequences: Guadalupe-Matarranya system (northern Spain) and
801 Wasatch Formation (western Colorado). *Geological Society of America Bulletin*, **112**,
802 1787–1803.

803 **Mohrig, D., and Smith, J.D.** (1996) Predicting the migration rates of subaqueous dunes. *Water*
804 *Resources Research*, **32**, 3207-3217.

805 **Nittrouer, J.A., Mohrig, D., Allison, M.A., and Peyret, A.-P. B.** (2011a) The lowermost
806 Mississippi River: a mixed bedrock-alluvial channel. *Sedimentology*, **58**, 1914-1934.

807 **Nittrouer, J.A., Mohrig, D., and Allison, M.** (2011b) Punctuated sand transport in the
808 lowermost Mississippi River. *Journal of Geophysical Research: Earth Surface*, **116**,
809 F04025.

810 **Nuse, B.** (2015) Flow processes and sedimentation in a low-sinuosity high net-sand content
811 fluvial channel belt: 3D outcrop study of the Cedar Mountain Formation, Utah.
812 *Unpublished MS Thesis, Colorado School of Mines.*

813 **Owen, A., Nichols, G.J., Hartley, A.J., Weissmann, G.S., and Scuderi, L.A.** (2015) Quantification
814 of a distributive fluvial system: The Salt Wash DFS of the Morrison Formation, SW U.S.A.
815 *Journal of Sedimentary Research*, **85**, 544-561.

816 **Paola, C., and Borgman, L.** (1991) Reconstructing random topography from preserved
817 stratification. *Sedimentology*, **38**, 553-565.

818 **Paola, C., Ganti, V., Mohrig, D., Runkel, A.C., and Straub, K.M.** (2018) Time not our Time:
819 Physical controls on the preservation and measurement of geologic time. *Annual Review*
820 *of Earth and Planetary Sciences*, **46**, 409-438.

821 **Parker, G., Paola, C., Whipple, K.X., and Mohrig, D.** (1998) Alluvial fans formed by channelized
822 fluvial and sheet flow. I: Theory: *Journal of Hydraulic Engineering*, **124**, 985-995.

823 **Parker, G., Wilcock, P.R., Paola, C., Dietrich, W.E., and Pitlick, J.** (2007) Physical basis for quasi-
824 universal relations describing bankfull hydraulic geometry of single-thread gravel bed
825 rivers. *Journal of Geophysical Research – Earth Surface*, **112**, F04005.

826 **Peterson, F., and Ryder, R.T.** (1975) Cretaceous rocks in the Henry Mountains region, Utah and
827 their relation to neighboring regions. in *Four Corners Geological Society Guidebook*, **8**, p.
828 166-189.

829 **Pizzuto, J.E.** (1987) Sediment diffusion during overbank flows. *Sedimentology*, **34**, 301–317.

830 **Reesink, A.J.H., and Bridge, J.S.** (2011) Evidence of bedform superimposition and flow
831 unsteadiness in unit-bar deposits, South Saskatchewan River, Canada. *Journal of*
832 *Sedimentary Research*, **81**, 814-840.

833 **Reesink, A.J.H., Van den Berg, J.H., Parsons, D.R., Amsler, M.L., Best, J.L., Hardy, R.J., Orfeo,**
834 **O., and Szupiany, R.N.** (2015) Extremes in dune preservation: Controls on the
835 completeness of fluvial deposits. *Earth-Science Reviews*, **150**, 652-665.

836 **Reesink, A.J.H.** (2018) Interpretation of cross strata formed by unit bars. In eds. M.Ghinassi, L.
837 Colombera, N.P. Mountney, and A.J.H. Reesink, *Fluvial Meanders and Their Sedimentary*
838 *Products in the Rock Record, International Association of Sedimentary Petrologists*
839 *Special Publication*, **48**, 173-200.

840 **Reitz, M.D., Jerolmack, D.J., and Swenson, J.B.** (2010) Flooding and flow path selection on
841 alluvial fans and deltas. *Geophysical Research Letters*, **37**, L06401.

842 **Rubin, D.M.** (1987) Cross-bedding, Bedforms, and Paleocurrents. *SEPM Concepts in*
843 *Sedimentology and Paleontology*, **1**.

844 **Rubin, D.M., and Hunter, R.E.** (1982) Bedform climbing in theory and nature. *Sedimentology*,
845 **29**, 121–138.

846 **Rubin, D.M., and Hunter, R.E.** (1987) Bedform alignment in directionally varying flows. *Science*,
847 **237**, 276-278.

848 **Sable, V.H.** (1956) Photogeologic map of the Tidwell-2 quadrangle, Emery and Grand counties,
849 Utah. *Miscellaneous Geologic Investigation, Map I-162*.

850 **Sadler, P.M.** (1981) Sediment accumulation rates and the completeness of stratigraphic
851 sections. *The Journal of Geology*, v. 89, 569-584.

852 **Sadler, P.M., and Jerolmack, D.J.** (2015) Scaling laws for aggradation, denudation and
853 progradation rates: the case for time-scale invariance at sediment sources and sinks.
854 *Geological Society of London, Special Publications, 404*, 69-88.

855 **Seminara, G., and Tubino, M.** (1989) Alternate bars and meandering: Free, forced and mixed
856 interactions. In S. Ikeda and G. Parker (Eds.), *River Meandering: Water Resources*
857 *Monograph, 12*, 267-320. American Geophysical Union: Washington, D.C.

858 **Shaw, J.B., and Mohrig, D.** (2014) The importance of erosion in distributary channel network
859 growth, Wax Lake Delta, Louisiana, USA: *Geology, 42*, 31-34.

860 **Skelly, R.L., Bristow, C.S., and Ethridge, F.G.** (2003) Architecture of channel-belt deposits in an
861 aggrading shallow sandbed braided river: the lower Niobrara River, northeast Nebraska.
862 *Sedimentary Geology, 158*, 249-270.

863 **Slingerland, R., and Smith, N.D.** (2004) River avulsions and their deposits. *Annual Review of*
864 *Earth and Planetary Sciences*, **32**, 257-285.

865 **Slingerland, R., and Williams, E.G.** (1979) Paleocurrent analysis in light of trough cross-
866 stratification geometry. *The Journal of Geology*, **87**, 724-732.

867 **Smith, N.D.** (1982) Some sedimentological aspects of planar cross-stratification in a sandy
868 braided river. *Journal of Sedimentary Petrology*, **42**, 624-634.

869 **Stokes, W.L.** (1961) Fluvial and Eolian Sandstone Bodies in Colorado Plateau. *AAPG SP-*
870 *Geometry of Sandstone Bodies*, **22**, 151–178.

871 **Stouthamer, E., and Berendsen, H.J.A.** (2001) Avulsion frequency, avulsion duration, and
872 interavulsion period of Holocene channel belts in the Rhine-Meuse Delta, the
873 Netherlands. *Journal of Sedimentary Research*, **71**, 589-598.

874 **Swanson, T., Mohrig, D., Kocurek, G., Perillo, M., and Venditti, J.** (2018) Bedform spurs: a
875 result of a trailing helical vortex wake. *Sedimentology*, **65**, 191-208.

876 **Swanson, T., Mohrig, D., Kocurek, G., Cardenas, B.T., and Wolinsky, M.A.** (2019) Preservation
877 of autogenic processes and allogenic forcings within set-scale aeolian architecture I:
878 numerical experiments. *Journal of Sedimentary Research*, **89**, 728-740.

879 **Swartz, J.M., Mohrig, D., Passalacqua, P., Goff, J., and Gulick, S.P.S.** (2018) From distributary to
880 tributary: coastal drainage network position and morphometry are set by depositional

881 processes. Presented at the American Geophysical Union 2018 Fall Meeting, EP21B-
882 2230.

883 **Van De Lagewag, W.Y., Van Dijk, W.M., and Kleinhans, M.G.** (2013) Channel belt architecture
884 formed by a meandering river. *Sedimentology*, **60**, 840-859.

885 **Wang, J., and Bhattacharya, J.P.** (2017) Plan-view paleochannel reconstruction of amalgamated
886 meander belts, Cretaceous Ferron Sandstone, Notom Delta, south-central Utah, U.S.A.
887 *Journal of Sedimentary Research*, **88**, 58–74.

888 **Whiting, P.J., and Dietrich, W.E.** (1993) Experimental constraints on bar migration through
889 bends: Implications for meander wavelength selection. *Water Resources Research*, **29**,
890 1091-1102.

891 **Williams, R.M.E., Irwin, R.P., and Zimelman, J.R.** (2009) Evaluation of paleohydrologic models
892 for terrestrial inverted channels: Implications for application to Martian sinuous ridges.
893 *Geomorphology*, **107**, 300–315.

894 **Williams, R.M.E., Chidsey Jr., T.C., and Eby, D.E.** (2007) Exhumed Paleochannels in Central
895 Utah—Analogues for Raised Curvilinear Features on Mars. *Central Utah-Diverse Geology of*
896 *a Dynamic Landscape*, 221–235.

897 **Wright, S., and Parker, G.** (2003) Grain-size specific suspended sediment transport and flow
898 resistance in large sand-bed rivers. In A. Gyr and W. Kinzelbach (Eds.), *Sedimentation*
899 *and Sediment transport*, 221-227. Netherlands: Springer.

900 **Wu, C., Bhattacharya, J.P., and Ullah, M.S.,** (2015) Paleohydrology and 3D facies architecture of
901 ancient point bars, Ferron Sandstone, Notom Delta, South-central Utah, USA. *Journal of*
902 *Sedimentary Research*, **85**, 399–418.

903 **Wu, C., Ullah, M.S., Lu, J., and Bhattacharya, J.P.** (2016) Formation of point bars through rising
904 and falling flood stages: Evidence from bar morphology, sediment transport and bed
905 shear stress. *Sedimentology*, **63**, 1458–1473.

906 **Young, R.G.** (1960) Dakota Group of Colorado Plateau. *American Association of Petroleum*
907 *Geologists Bulletin*, **44**, 158-194.

908 **Zaki, A.S., Pain, C.F., Edgett, K.S., and Giegengack, R.** (2018) Inverted stream channels in the
909 Western Desert of Egypt. Synergistic remote, field observations and laboratory analysis
910 on Earth with applications to Mars. *Icarus*, **309**, 105-124.

911

912

913

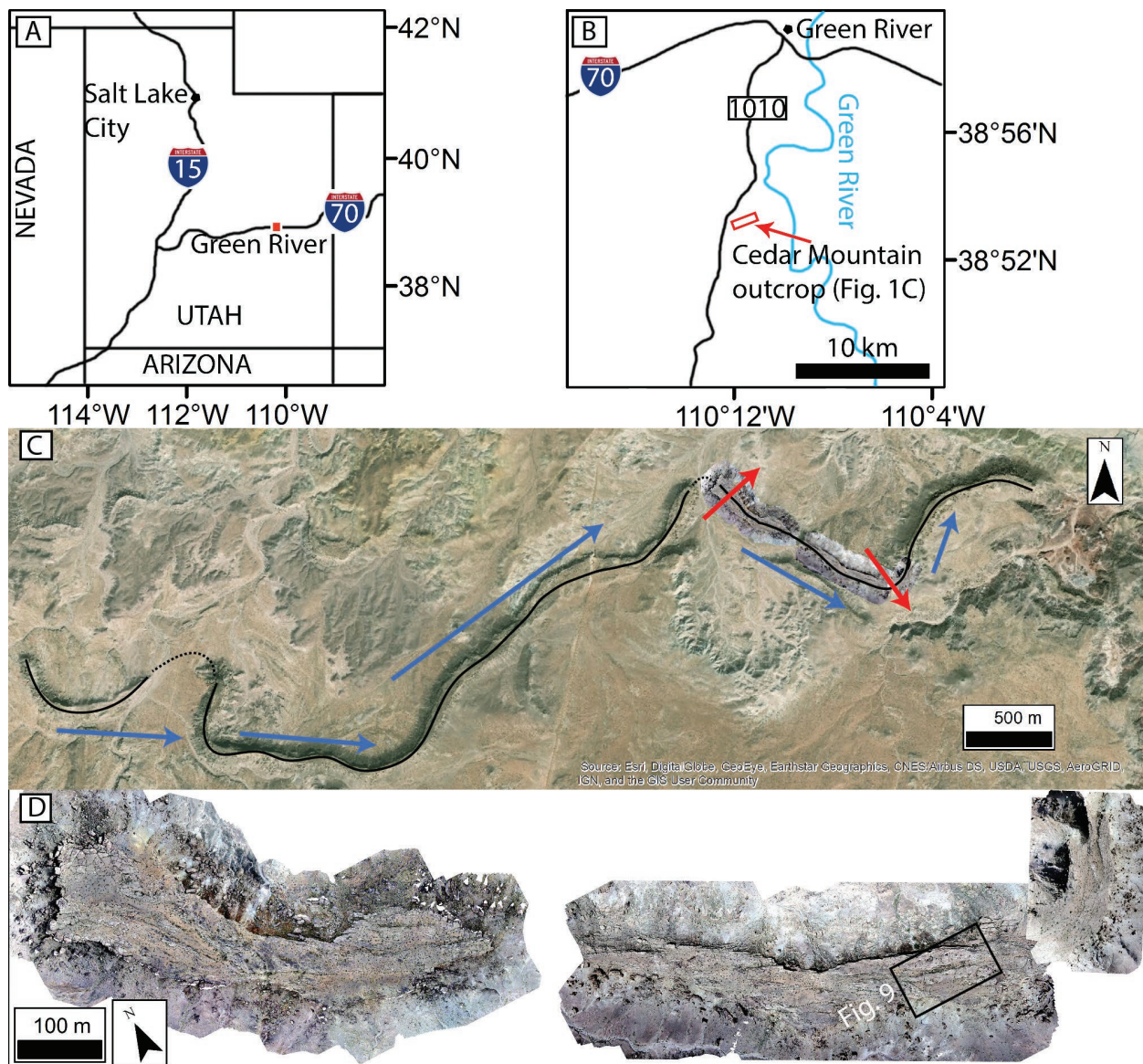
914

915

916

917

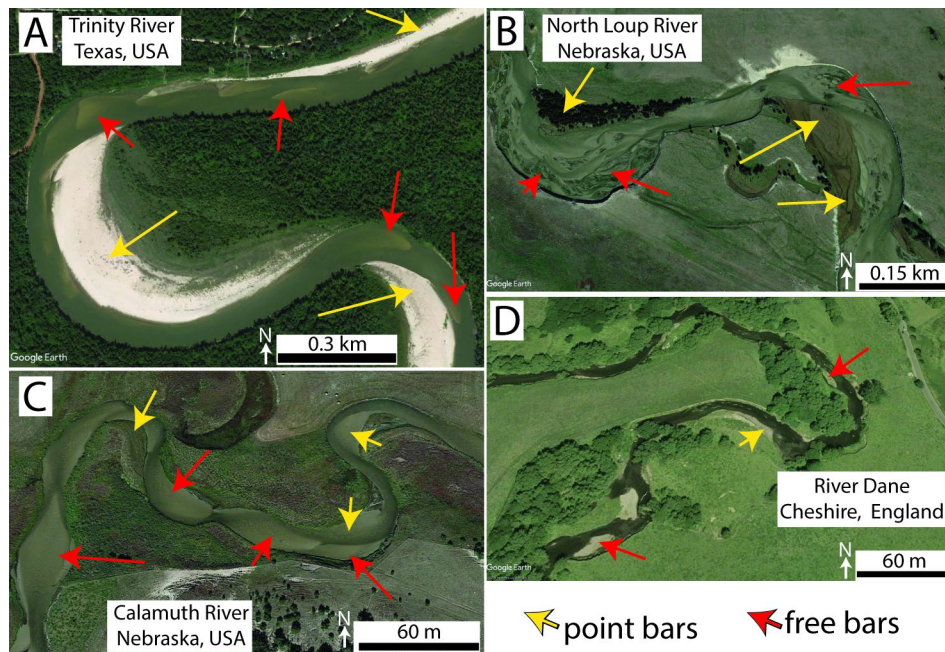
918 **FIGURE CAPTIONS**



919
920 Figure 1 – (A) Index map of Utah. (B) Enlargement near Green River, showing the location of the
921 town as well as the studied ridges of the Ruby Ranch Member of the Cedar Mountain
922 Formation. (C) View showing the ridges beyond the study area. Black line maps out a ridge
923 centerline for several km, with interpreted dashed segments bridging erosional discontinuities.
924 Blue arrows show the general direction of paleoflow. Red arrows mark the two major bends

925 bounding the studied part of the ridge. The arrows point away from the center of curvature,
 926 and match with the general dip directions of local dipping bar strata. (D) Drone ortho-images of
 927 the studied eastern and western ridges of the Ruby Ranch Memberridges. The photomosaics
 928 are rotated slightly to fit the panel, but are correctly co-located.

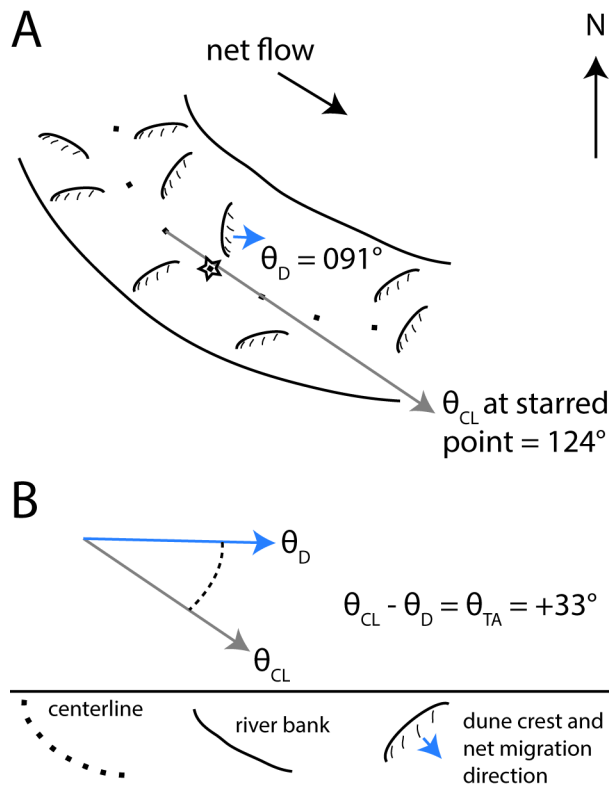
929



931 Figure 2 – Free bars (red arrows) and point bars (yellow arrows) commonly coexist in rivers,
 932 both in straight reaches and bends. (A) Trinity River, Texas, USA. Image centered at 30.134° N, -
 933 94.815° E. (B) North Loup River, Nebraska, USA. Image centered at 42.019° N, -100.098° E. (C)
 934 Calamuth River, Nebraska, USA. Image centered at 42.083° N, -99.649° E. (D) River Dane,
 935 Cheshire, England. Image centered at 53.183° N, -2.259° E.

936

937



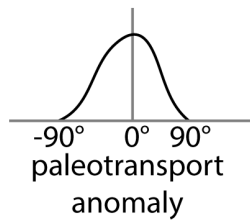
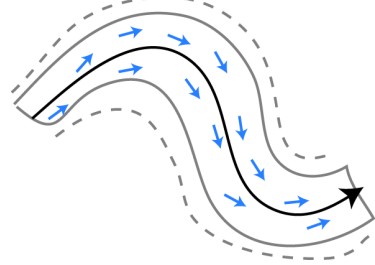
938

939 Figure 3 – (A) Diagram defining the components of the transport anomaly, θ_{TA} , for a modern
 940 river channel. A measurement of transport direction, θ_D , is made from the orientation of a
 941 dune crest (short black arrow; 091°). The centerline point closest to the measurement of θ_D is
 942 starred. The orientation of the starred centerline point, θ_{CL} , is defined as the azimuth direction
 943 of the ray originating at the adjacent upstream point and passing through the adjacent
 944 downstream point (gray arrow; 124°). (B) The transport anomaly, θ_{TA} , is defined as $\theta_{CL} - \theta_D$. It
 945 may be positive or negative, and is bound between -180° and positive 180° . In this scenario, θ_{TA}
 946 = $124^\circ - 091^\circ = 33^\circ$.

947

948

A: Minimum lateral amalgamation, non-random erosion pattern



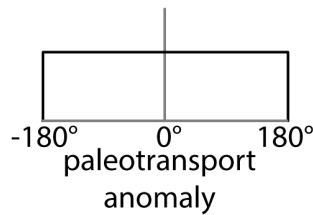
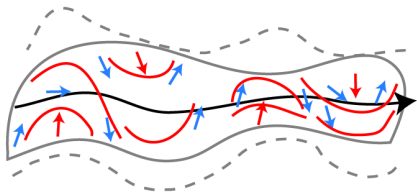
$$\sigma_{\text{ancient}} \approx \sigma_{\text{modern}}$$

$$\text{mean}_{\text{ancient}} \approx 0$$

with increasing amalgamation values will deviate until

distribution approaches random

B: Significant lateral amalgamation, non-random erosion pattern



↑ paleotransport direction

↑ bar strata dip direction

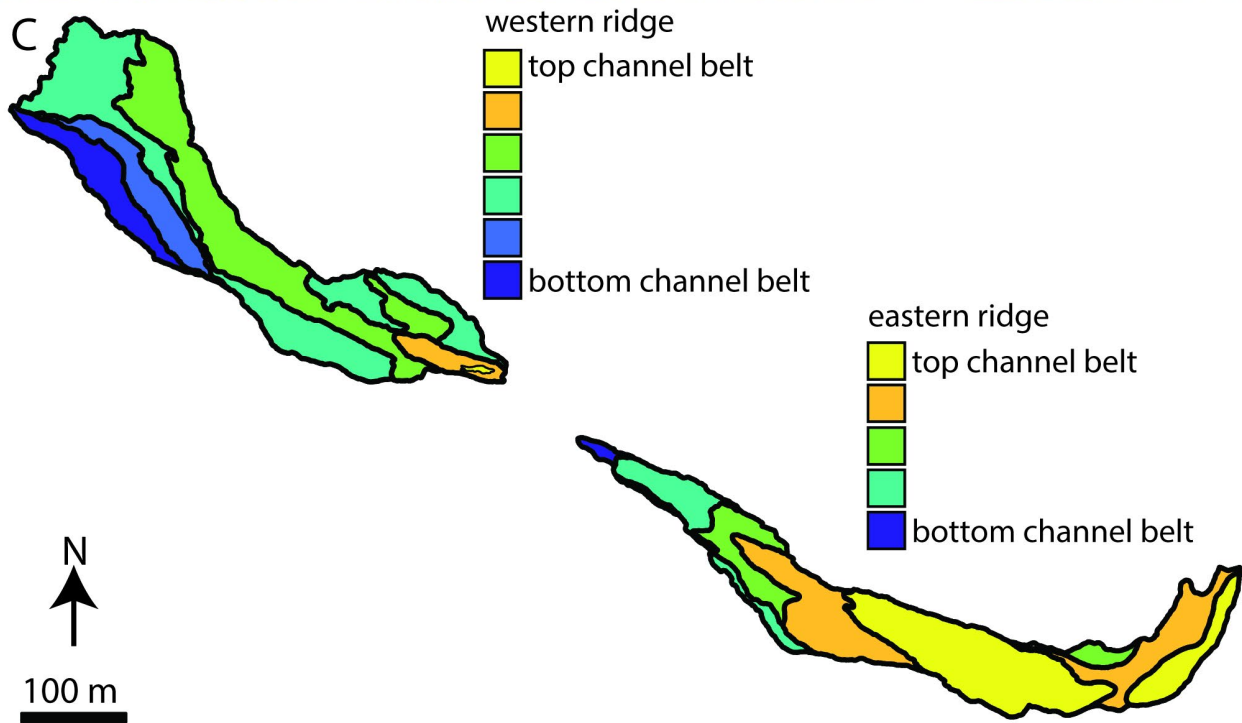
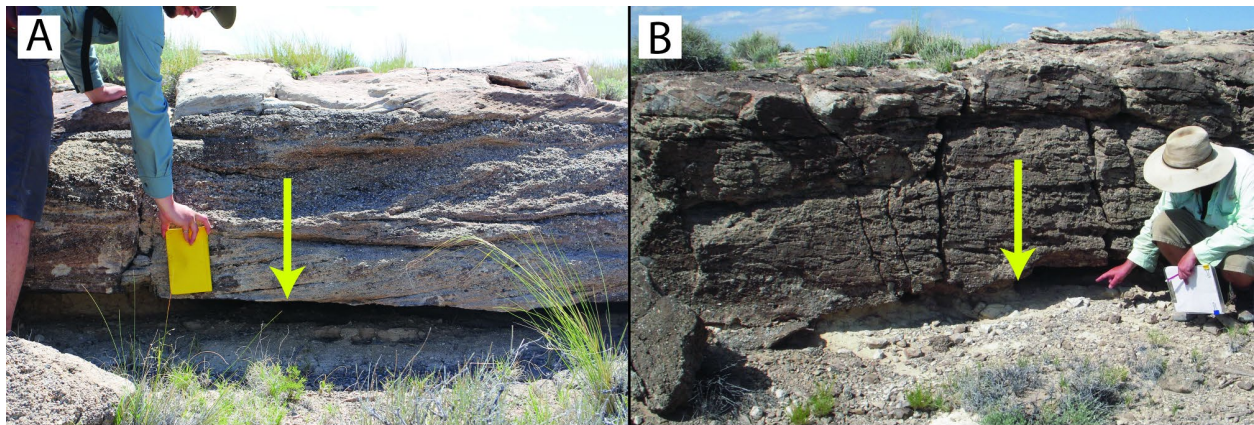
↪ bar accretion strata

↪ ridge centerline

ridge outline (solid) and prior belt extent before erosion (dashed)

949

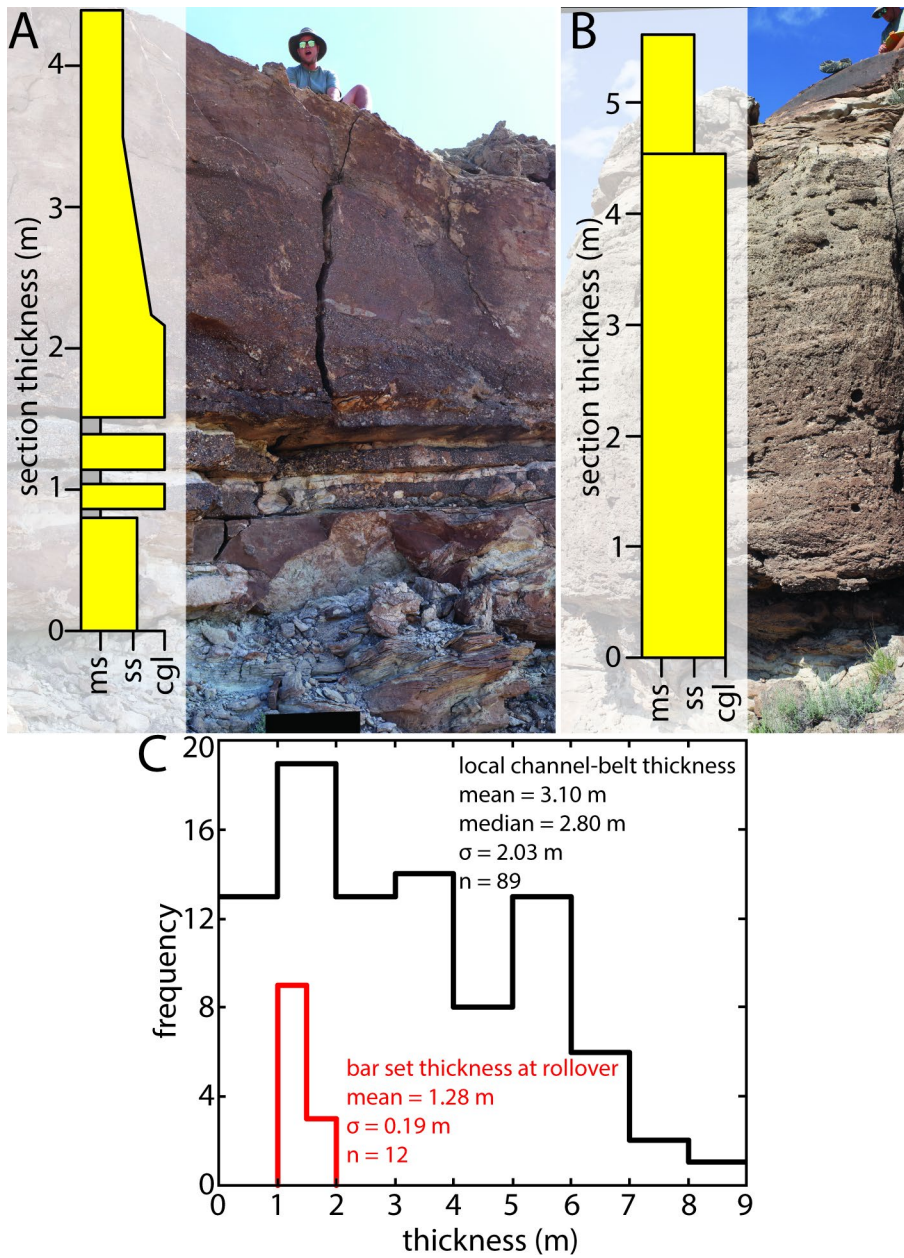
950 Figure 4 – Hypothesized scenarios guiding interpretations of paleotransport anomaly results.
 951 Schematic diagrams are on the left, the distribution of paleotransport anomaly measurements
 952 are in the middle, and relevant statistical moments are on the right. Standard deviation is
 953 shown by σ . Legend is at the bottom. (A) The ridge centerline represents well the formative
 954 channel centerline. With increasing lateral amalgamation, results will instead approach the
 955 scenario in panel B. (B) Lateral amalgamation of the channel-belt separates any formative
 956 channel centerline from the ridge centerline. Laterally accreting bar strata are preserved. A
 957 random exhumation pattern not following the edges of the channel belt is unlikely to show any
 958 of these patterns.



959

960 Figure 5 – (A-B) Yellow arrows pointing to erosional surfaces above friable, recessed mudstones
 961 separating coarse-grained, cross-bedded packages. These erosional surfaces are interpreted to
 962 represent the contacts between stacked channel belts. (C) Geologic maps showing the stacking
 963 patterns of channel-belts exposed at the surface of both ridges. There is no attempt to
 964 correlate individual channel belts between ridges.

965



966

967 Figure 6 – (A) Vertical section showing story-bounding surfaces and associated mudstones.

968 Stories in this section are of average to below-average thickness. (B) Two stories bounded by an

969 erosional surface with no associated mudstone. The bottom story is above average thickness.

970 (C) Histogram of local channel-belt (story) thicknesses measured from vertical sections, and the

971 mean thickness of a bar set at the rollover (red line), which is used as a proxy for channel depth.

972 The difference between channel depth and channel-belt thickness is due to aggradation of the
973 channel bed.

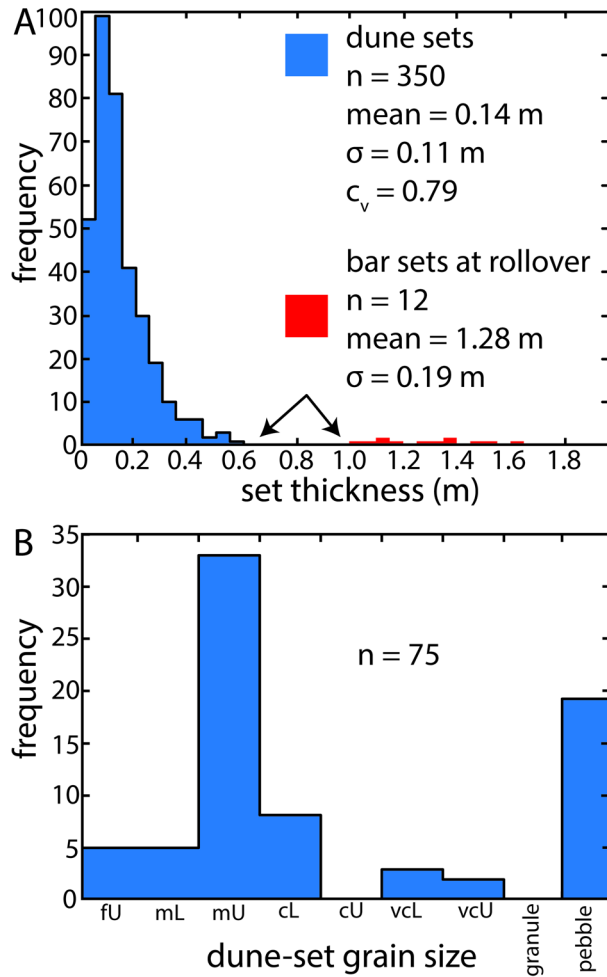
974



975

976 Figure 7 - Photo of dune cross strata exposed in planview along upper ridge surfaces. Blue
977 arrow shows the mean dip directions of cross strata. This 3-D outcrop shows the relationship
978 between planform-exposed cross strata and vertically exposed cross strata. Boots for scale.

979

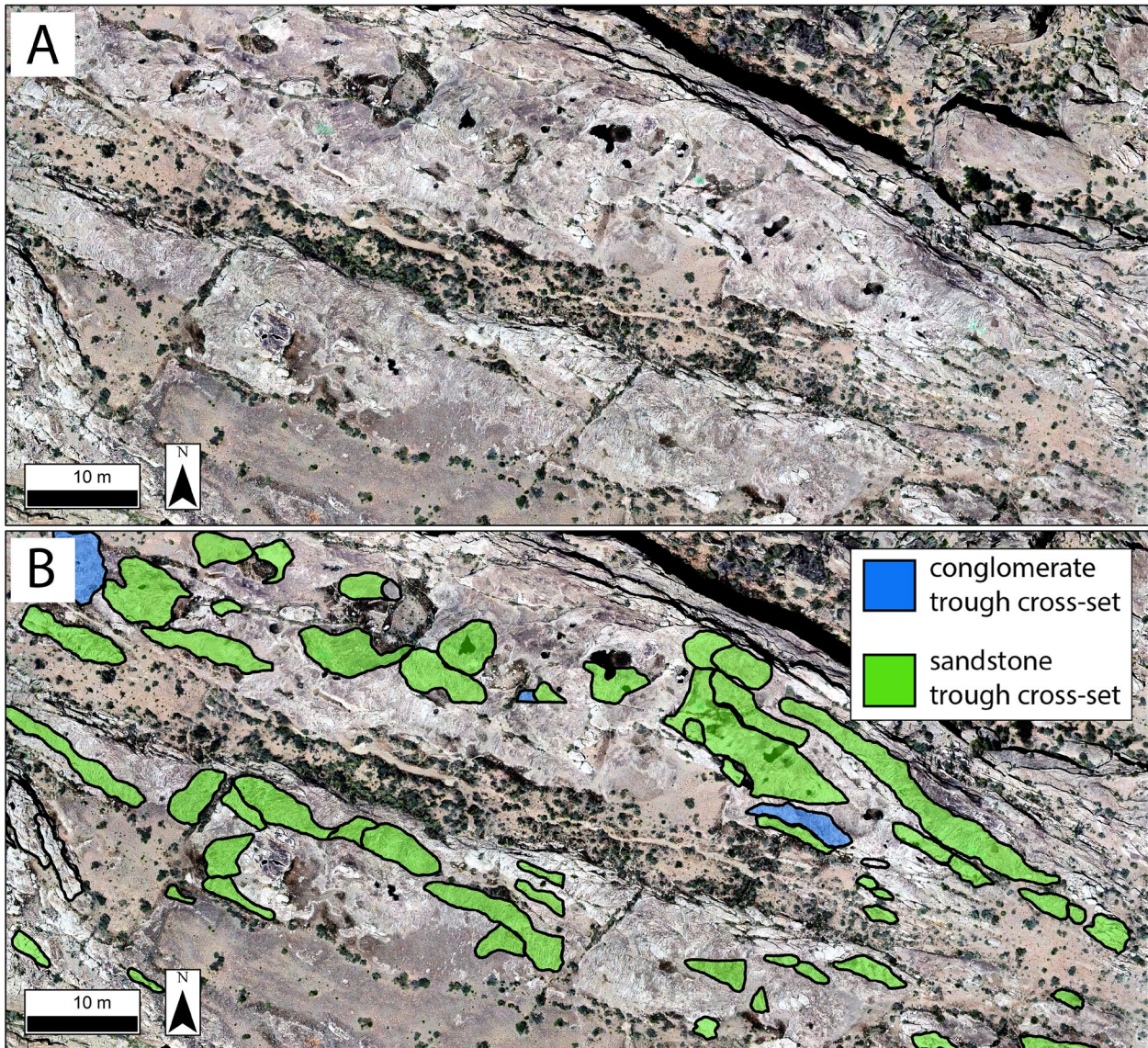


980

981 Figure 8 – (A) Histograms showing the distribution of dune and bar cross-set thicknesses, with
 982 statistical moments and the coefficient of variation (c_v). Arrows highlight a break between the
 983 two distributions when measuring bar sets at a rollover. (B) Distribution of grain-size classes in
 984 dune cross sets. Classes labeled fu, mL, mU, cL, cU, vcl, and vcU represent sand sizes of fine
 985 upper, medium lower, medium upper, coarse lower, coarse upper, very coarse lower, and very
 986 coarse upper, respectively.

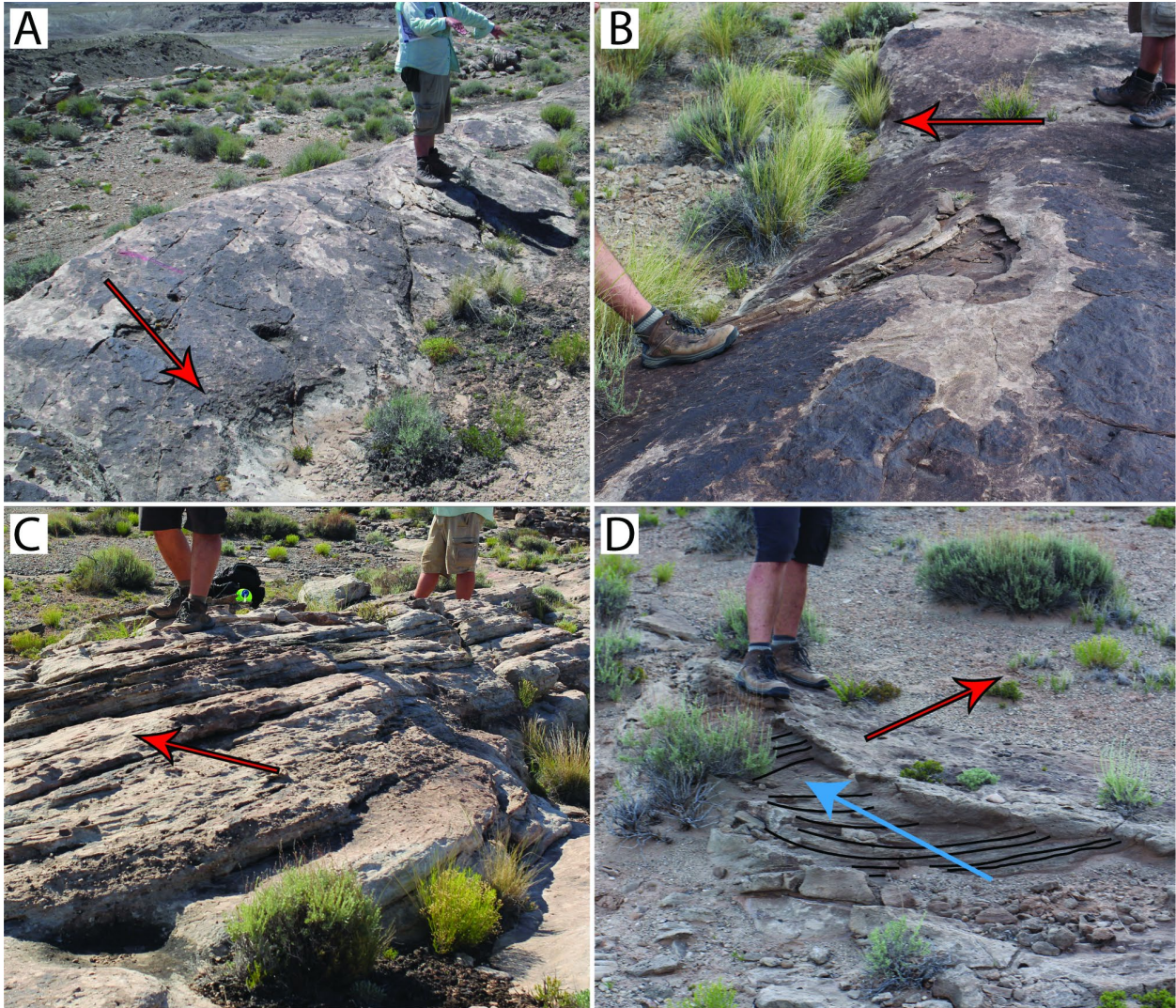
987

988



989

990 Figure 9 – (A) Example of drone photomosaics used as field base maps. (B) Digitized field map
991 showing planform-exposed sets of cross strata outlined and filled in with green (sandstone) or
992 blue (pebble conglomerate).



993

994

Figure 10 - Examples of larger-scale accretion strata. Red arrows show the dip direction of the

995

strata in each panel. (A) A lack of exposed bounding surfaces on this topographic surface

996

suggests the topography itself represents a bounding surface. (B) Beneath the arrow, erosion

997

exposes internal stratification parallel to the surface. (C) A 3-D outcrop of larger-scale dipping

998

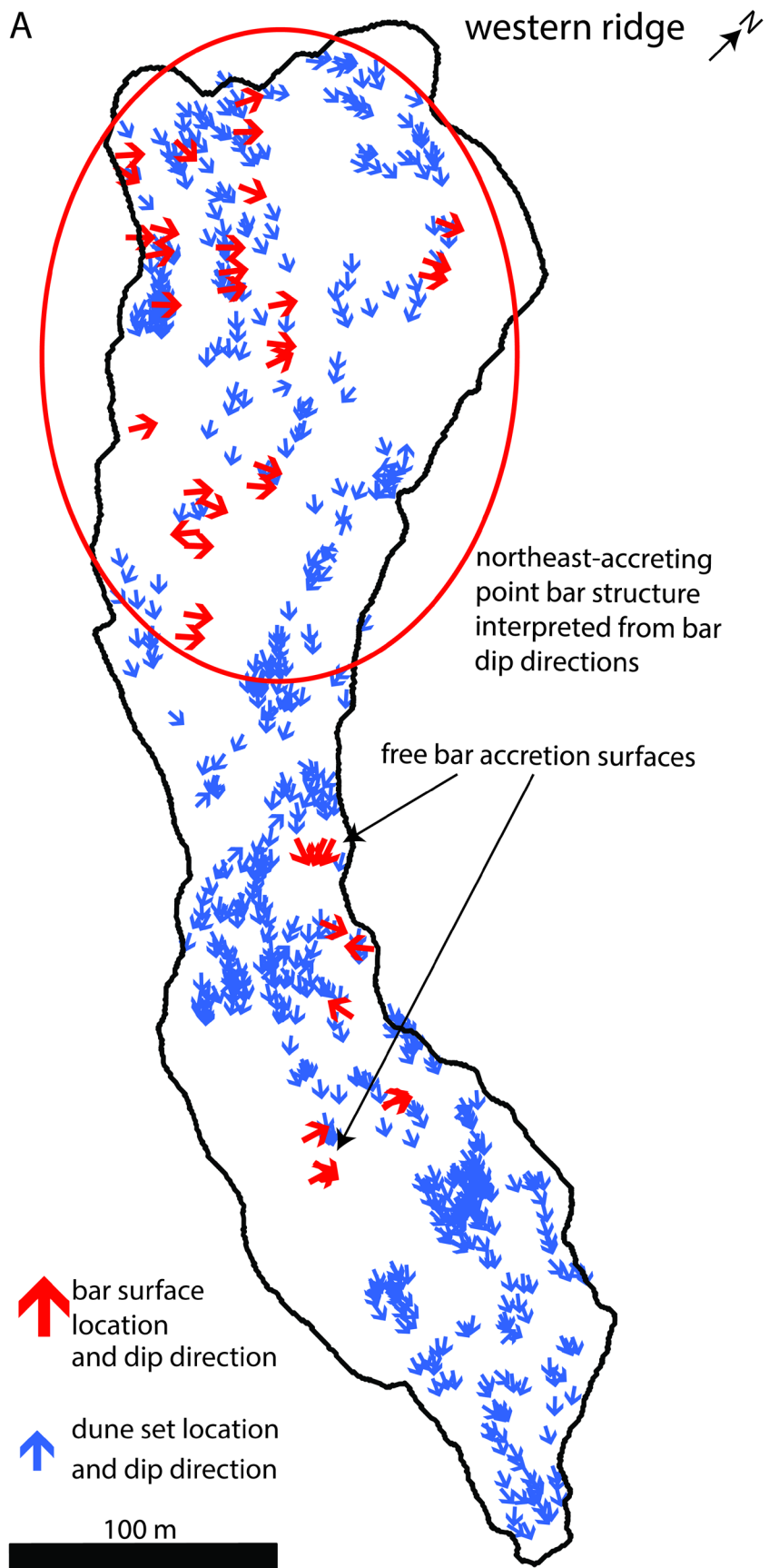
strata composed of smaller-scale stratification exposed by erosion. (D) Compound cross strata

999

with a larger-scale accretion surface (red arrow) dipping obliquely to a smaller-scale dune set

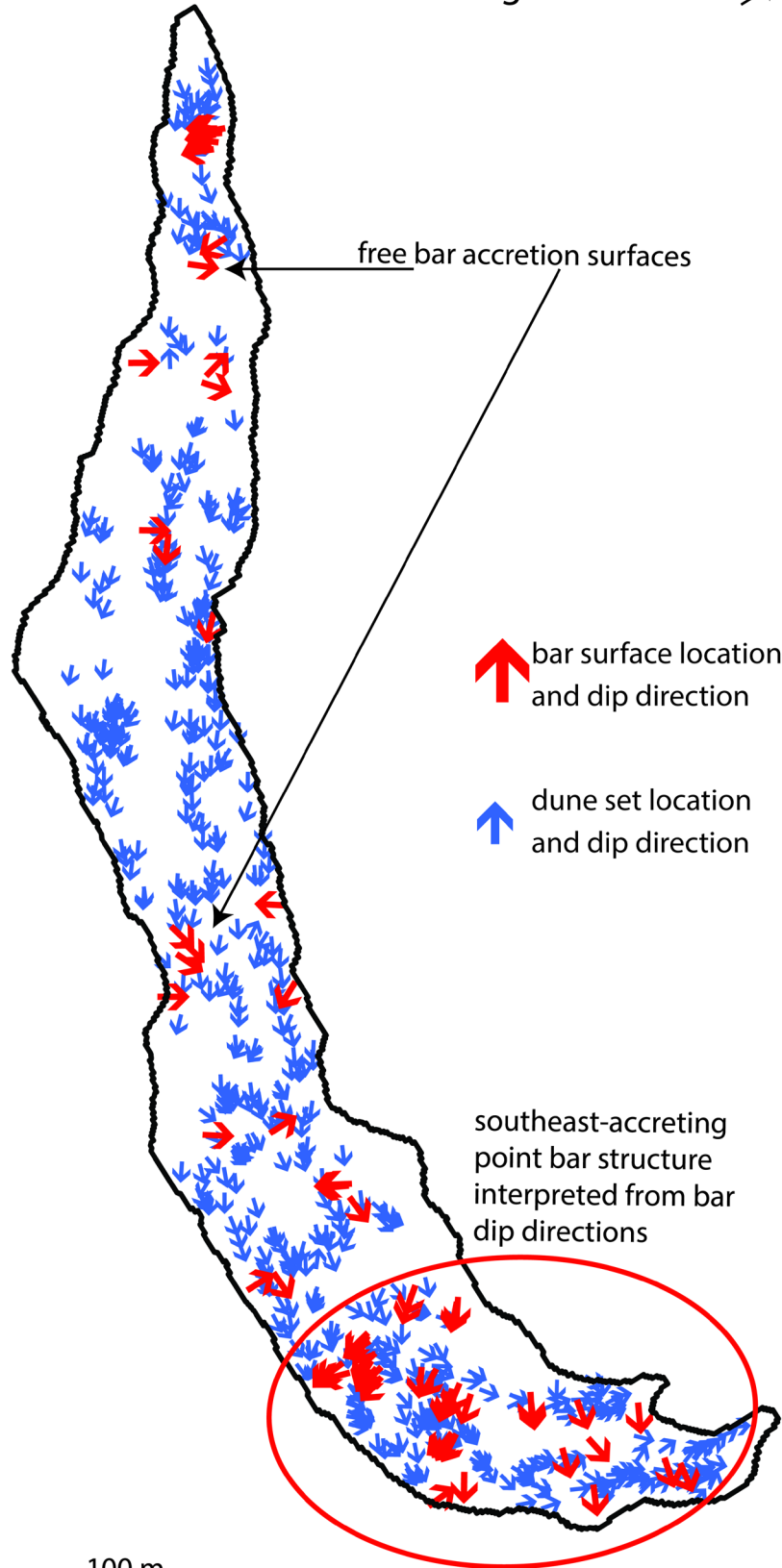
1000

(blue arrow). A few dune cross strata are mapped in black lines.



B

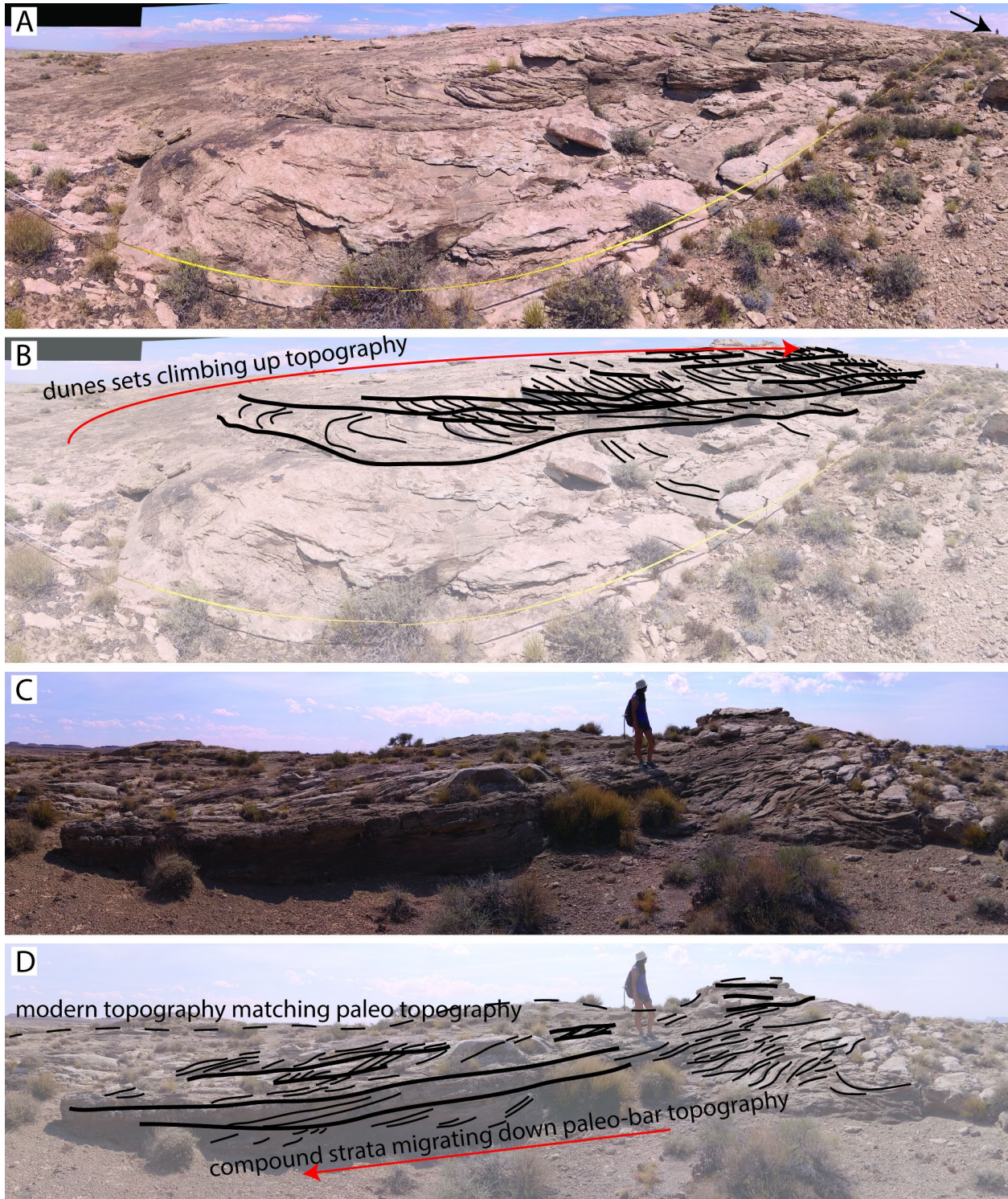
eastern ridge



100 m



1003 Figure 11 – Planform maps outlining the top surfaces of the western (A) and eastern (B) ridges.
1004 Two locations with clusters of similarly dipping bar accretion surfaces following ridge curvature
1005 are interpreted to represent point bars. The northeast-accreting point bar structure of the
1006 western ridge corresponds with a larger-scale ridge curvature beyond the extent of the study
1007 area (Fig. 1C). Bar accretion surfaces not clearly associated with a point bar are interpreted as
1008 free-bar accretion surfaces.

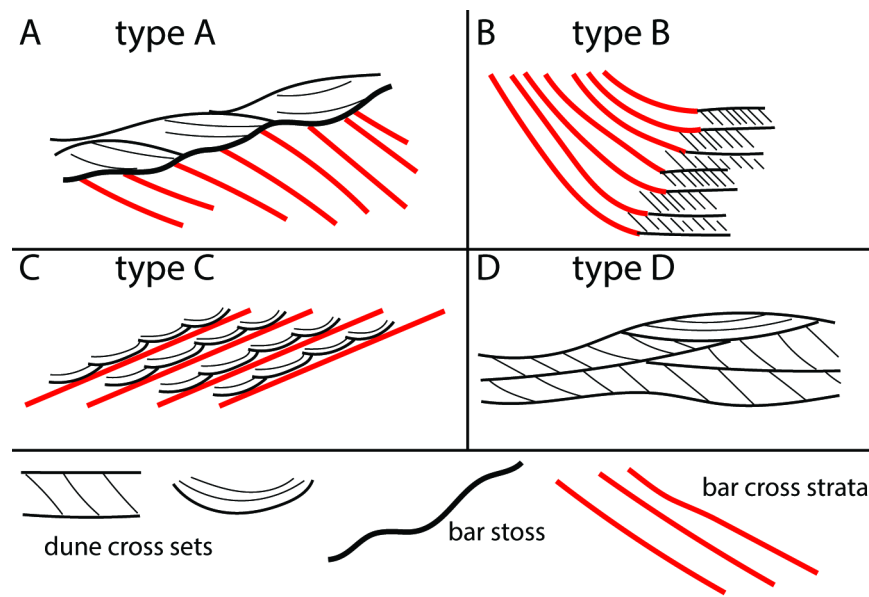


1009

1010 Figure 12 – The preservation of bar topography on upper-ridge surfaces. (A) Fisheye view of a

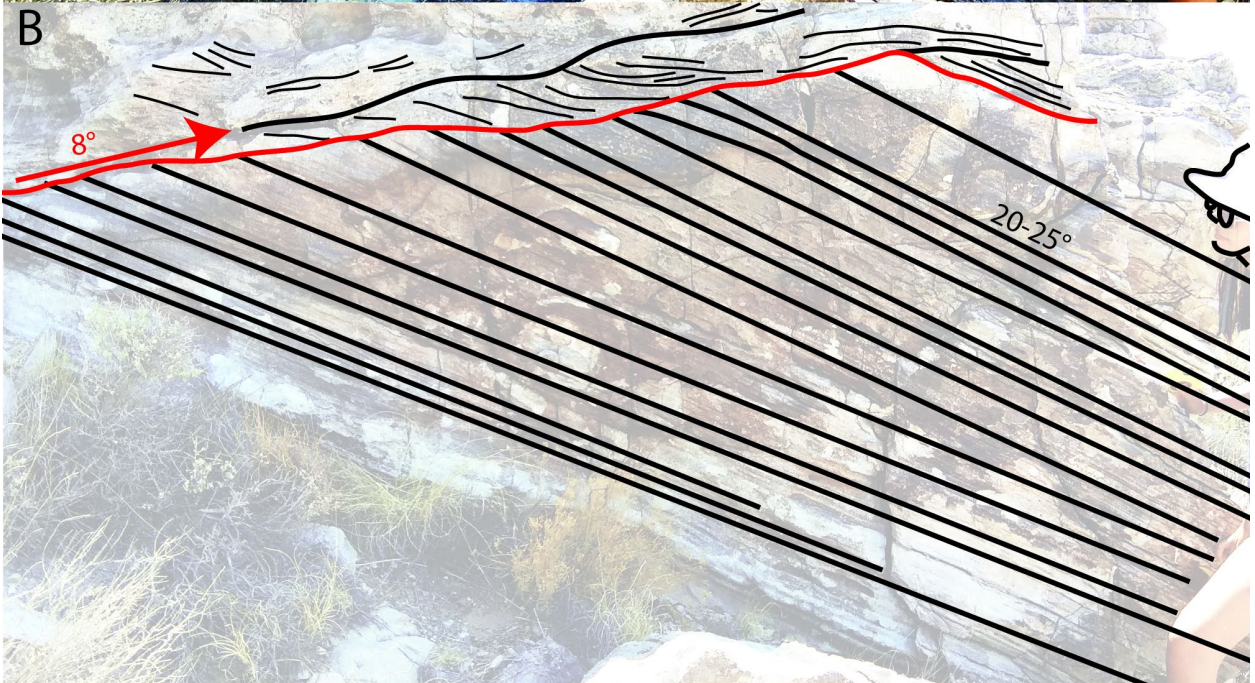
1011 sandstone mound rising towards the downstream direction (left to right), with a surface

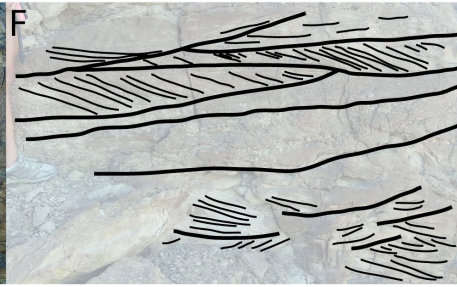
1012 defined by shingled cross-sets climbing with topography. This is interpreted as the stoss surface
 1013 of a downstream-migrating barform. Tape measure for scale in foreground, arrow pointing to
 1014 person in background. (B) Interpretation of panel A. (C) Downstream end of sandstone mound
 1015 featuring cross sets and topography falling in the downstream direction. Interpreted as the lee
 1016 slope of a downstream-migrating barform. Person for scale (1.65 m tall). (D) Interpretation of
 1017 panel C.



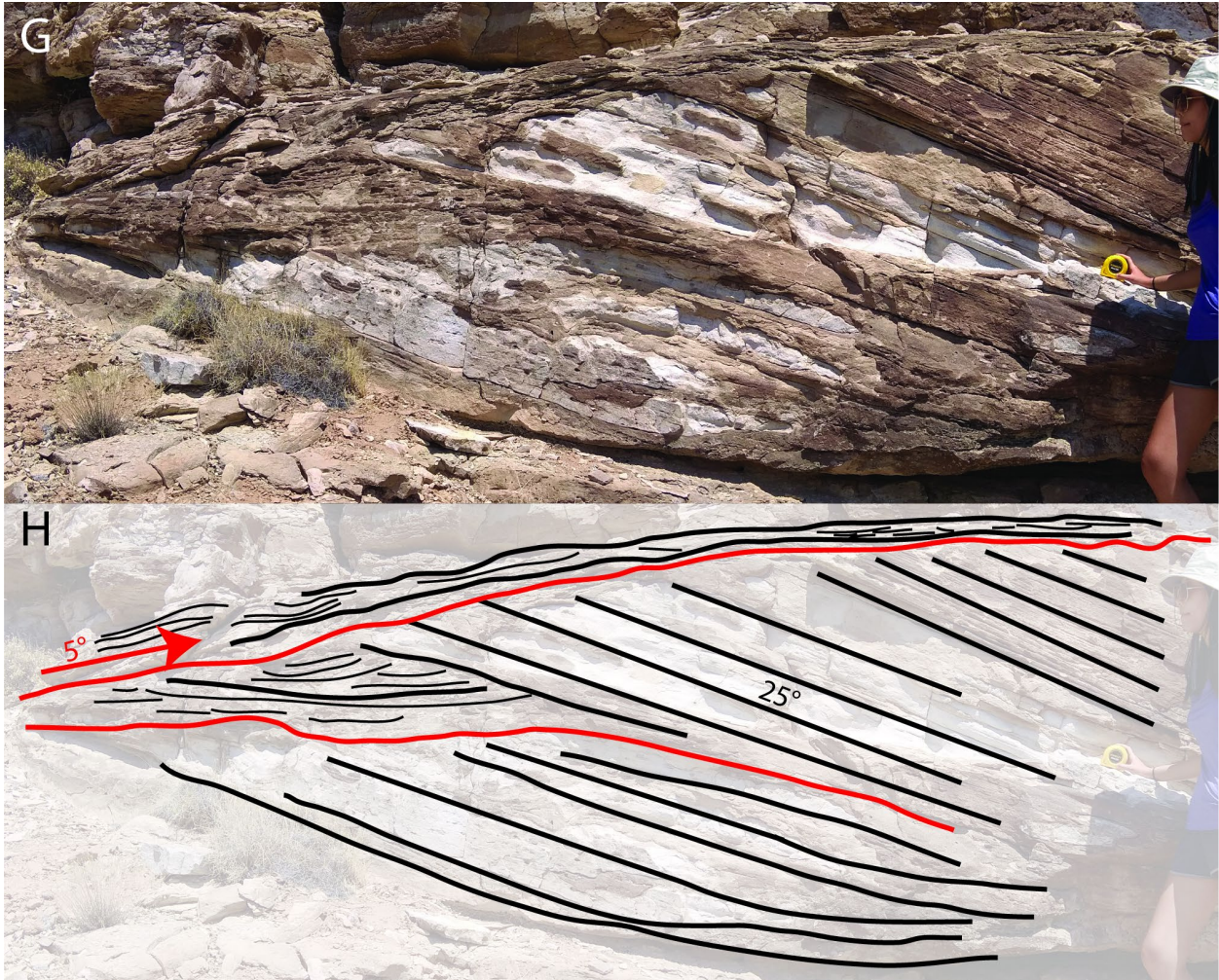
1018
 1019 Figure 13 – The four arrangements of compound dune and bar strata. A: Type A strata have a
 1020 bar set beneath dune cross-sets, separated by an upstream-dipping surface. Bar strata are not
 1021 necessarily at angle of repose in this figure. B: Type B strata have bar sets shallowing and
 1022 thickening downstream, where they conformably become dune cross sets. C: Type C strata
 1023 show compound dune and bar strata dipping at high angles to each other. D: Type D strata are
 1024 dune sets with no clear compound structure.

1025
 61





1027



1028

1029 Figure 14 - Cross-sectional view of Type A-D strata (Fig. 13), with superimposed interpretations.

1030 Sets of dune and bar strata are marked by thick black lines and dune cross strata by thinner

1031 black lines. Surfaces separating dune and bar strata are marked by red lines. (A-B) Type A strata

1032 from the stoss side of a bar, with an interpreted transition to the lee side. Flow was from left to

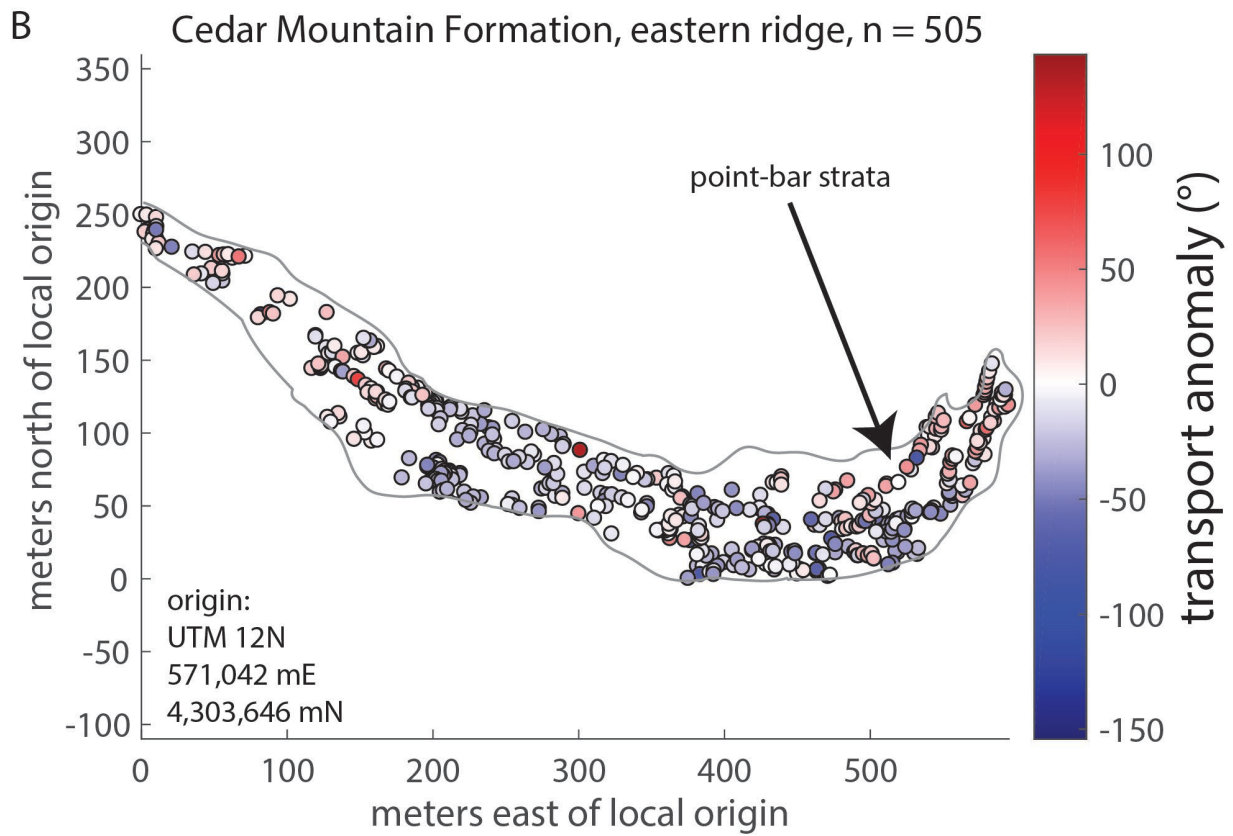
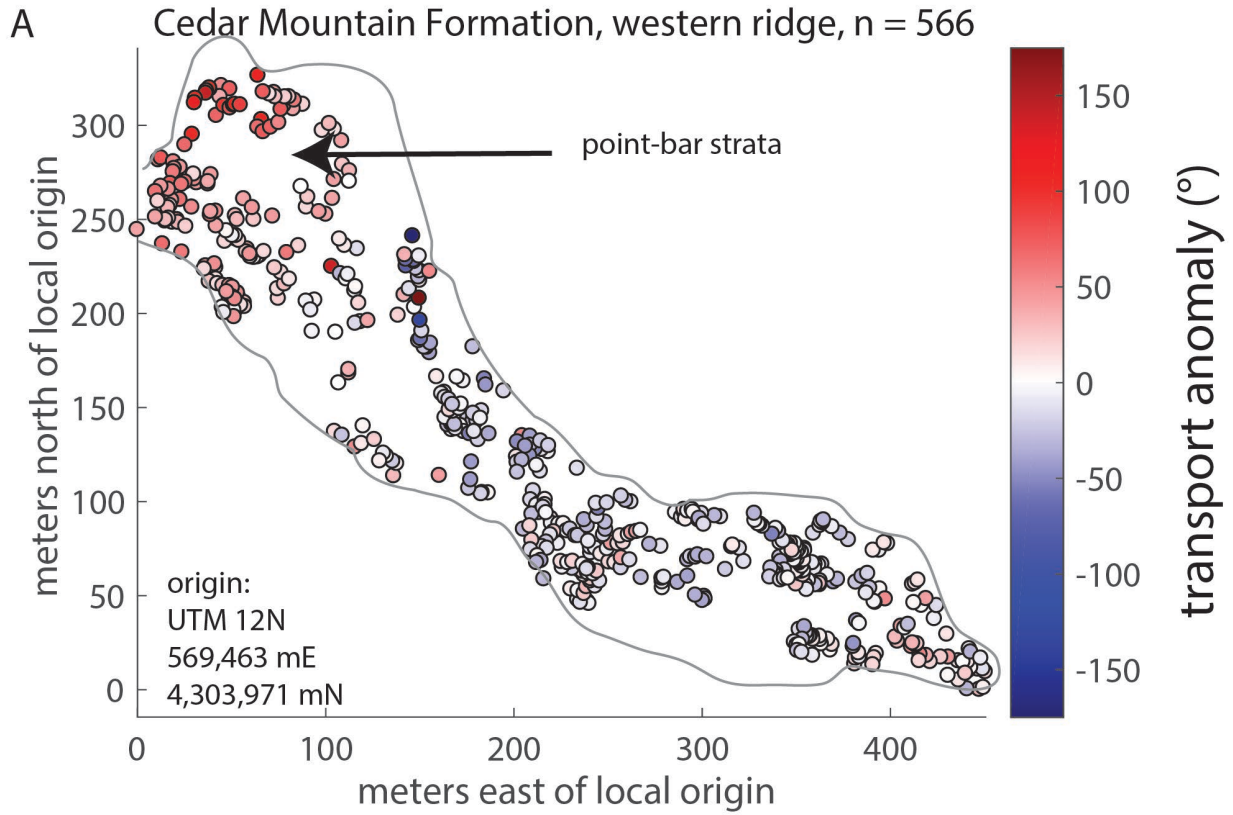
1033 right. (C-D) Cross-sectional view of preserved strata from the lee (Type B) and stoss (Type A)

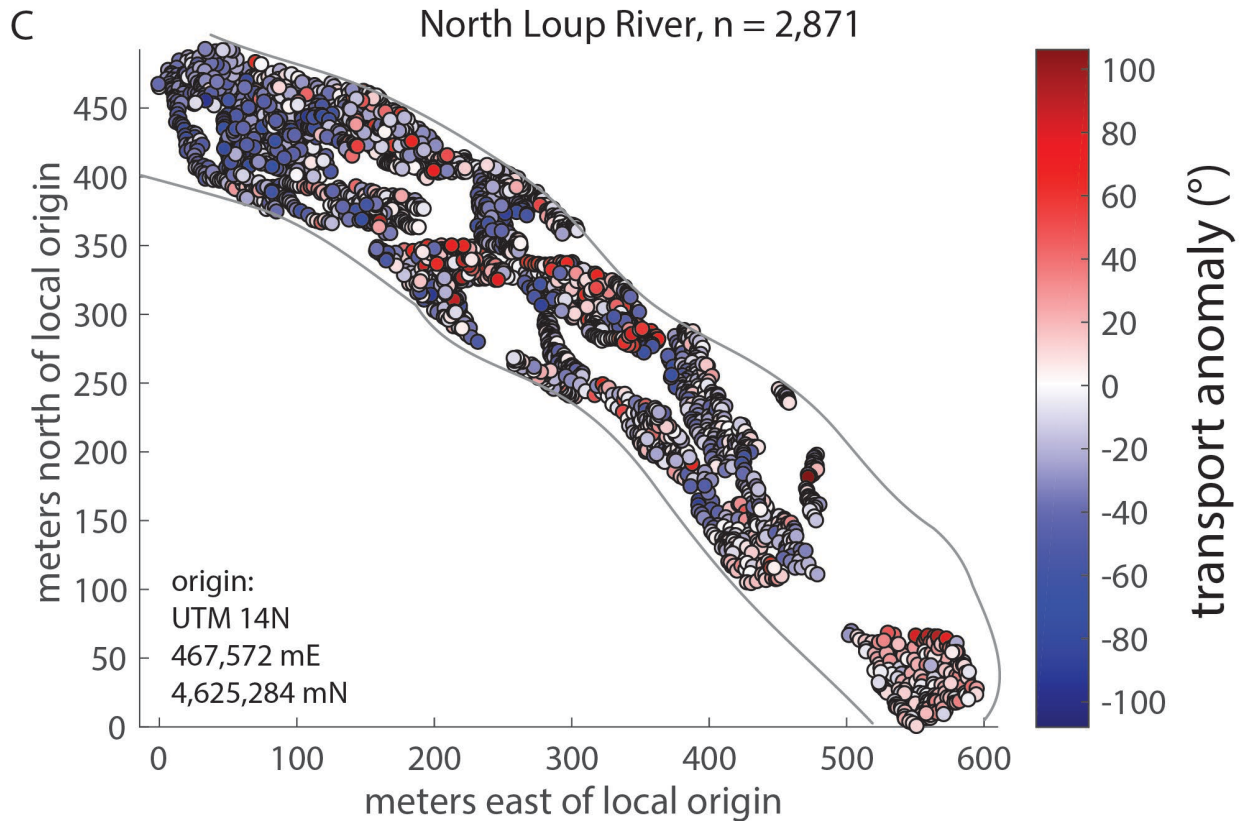
1034 sides of a bar form. Flow was from right to left. (E-F) Cross-sectional view of Type D strata

1035 featuring a $\pm 90^\circ$ spread in transport direction, conglomerates, and a lack of bar architecture.

1036 This type of architecture is interpreted as a thalweg environment due to the coarser grains

1037 driven by higher velocity flow, and a larger spread in transport driven by changes in steering
1038 due to bar growth. (G-H) Cross-sectional view showing the internal structure of a barform with
1039 Type A strata overlying Type B strata. Flow was from left to right. From bottom to top, the
1040 transition from stoss-to-lee architecture to lee architecture, all within the same barform,
1041 records the forward migration and aggradation of the barform.





1043

1044 Figure 15 – Transport anomaly maps of the western ridge of the Ruby Ranch Member (A), the

1045 eastern ridge (B), and the North Loup River (C). X and Y coordinates are relative to a different

1046 local datum in each map, shown in the bottom left corner of each panel. Circles show the

1047 location of paleotransport or modern transport direction measurements. The color at each

1048 point represents the paleotransport or transport anomaly (Fig. 3A-B). Colors are stretched to

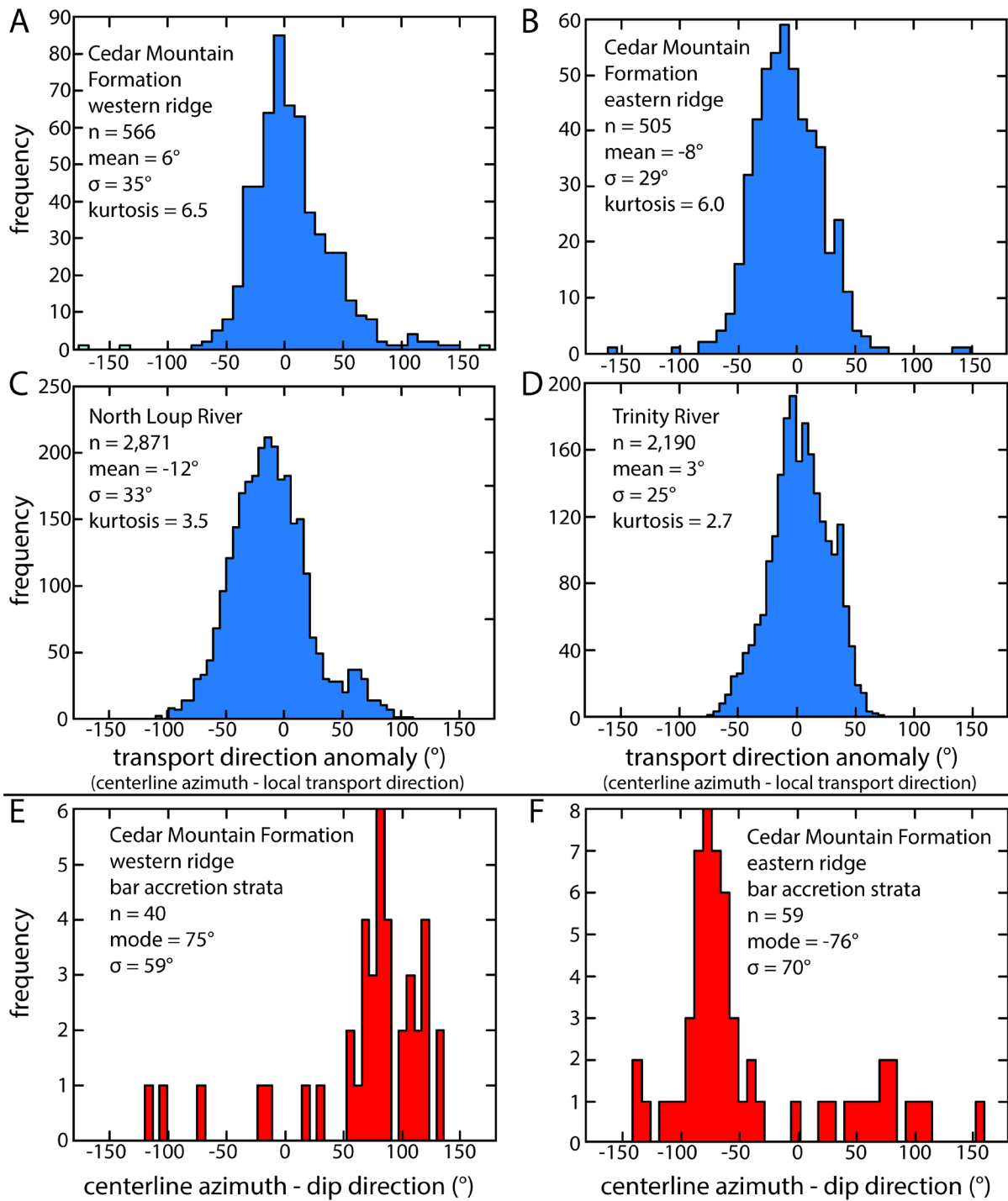
1049 each individual panel. Gray lines represent ridge outlines and the banks of the North Loup

1050 River. Black arrows in panels A and B point to regions recording point bar accretion, and are

1051 associated with relatively high anomaly values, particularly in the western ridge (Figs. 1C and

1052 11).

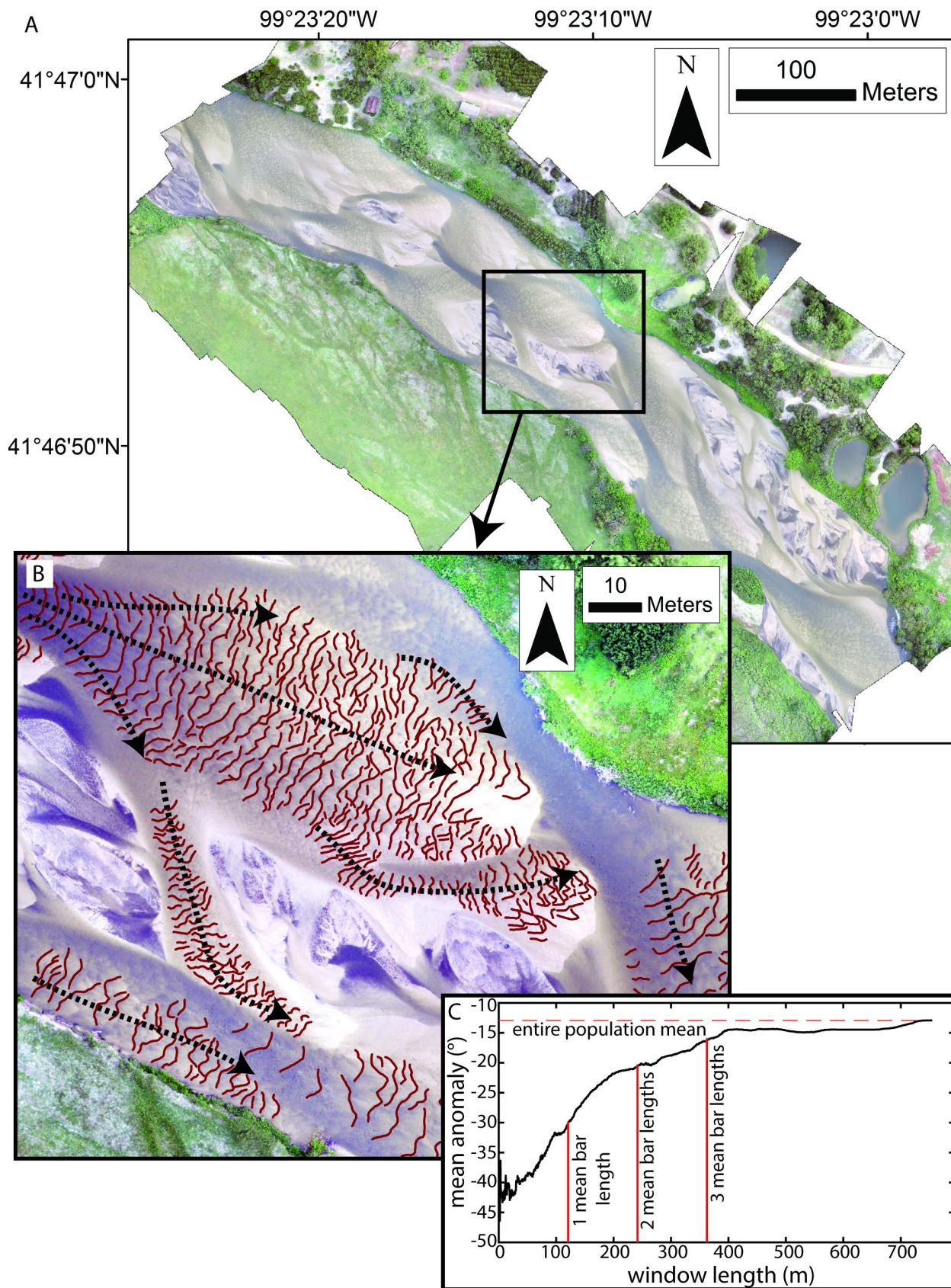
1053



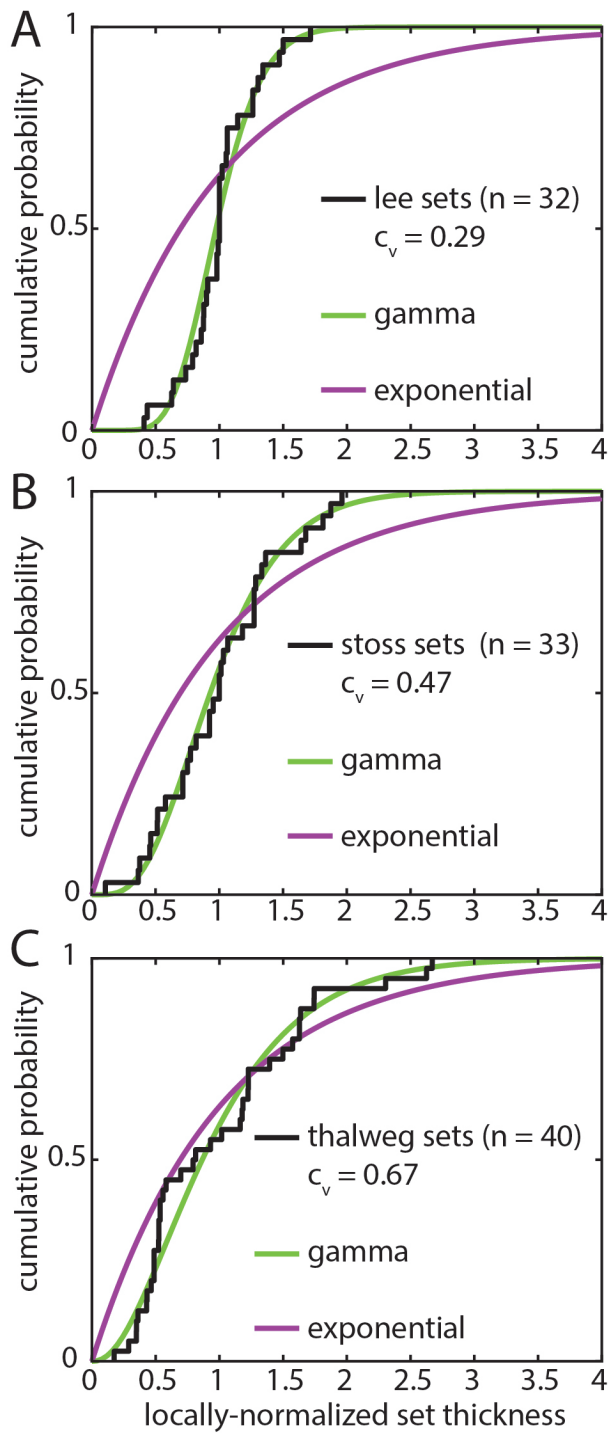
1054

1055 Figure 16 – Histograms showing the distribution of paleotransport/transport anomalies of the
 1056 western (A) and eastern (B) ridges of the Ruby Ranch Member, and the modern North Loup
 1057 River (C) and Trinity River (D). The number of measurements, mean, and standard deviation are

1058 reported in each panel. Note the similarity in mean and standard deviation between the
1059 ancient and modern datasets. Histograms (E) and (F) show the difference between dip
1060 directions of bar accretion strata exposed along the upper surfaces of ridges and the centerline.
1061 Both histograms show a wide distribution of values with peaks approaching perpendicular to
1062 the centerline trend.



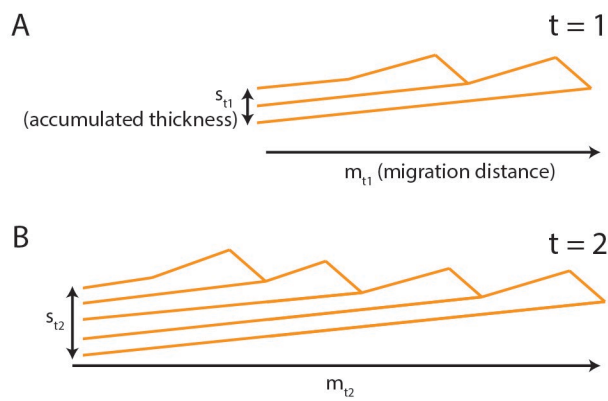
1064 Figure 17 – (A) Drone photomosaic of the North Loup River near Taylor, Nebraska, USA
1065 (Swanson et al., 2018). Brighter tan colors within the channel are subaqueous and represent
1066 higher portions of downstream-migrating bars beneath shallow water. Darker reaches of the
1067 channel represent deeper water. Mixed white and black areas with no crestlines mapped are
1068 subaerially exposed bar tops that are not currently undergoing fluvial transport. The location of
1069 panel B is shown in the black box. (B) Enlargement showing dune crestlines (short red lines)
1070 interpreted as perpendicular to dune transport direction. Black dashed arrows show general
1071 trends in local transport directions due to the steering of flow around bars. (C) Window length
1072 vs. the mean transport anomaly within the window. As the window length approaches that of
1073 the ~ 3 barforms or about half the reach, the sampled mean approaches the mean of the entire
1074 reach, indicating the total variability has been adequately sampled. Changes in curvature of this
1075 line are observed near multiples of mean bar length, supporting topographic steering as the
1076 source of the transport anomaly.



1077

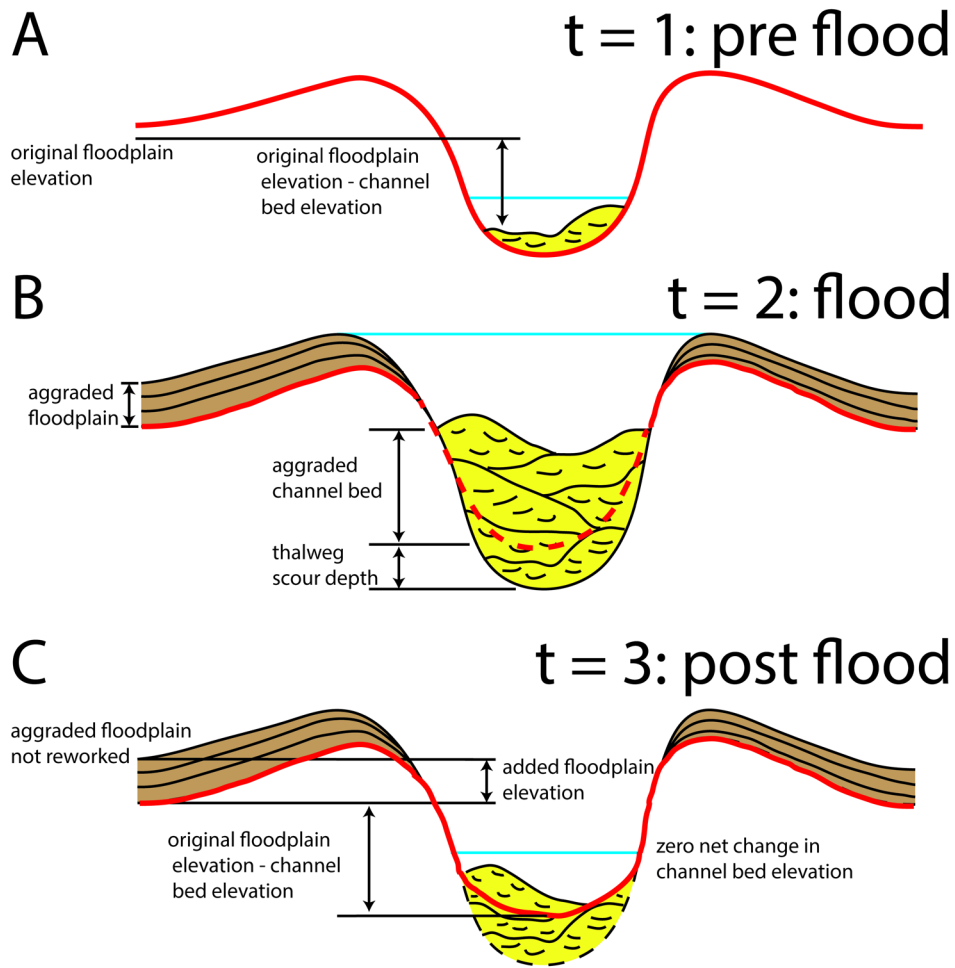
1078 Figure 18 – (A) Cumulative distribution function (CDF) showing the mean- standardized
 1079 distribution of set thickness located within bar lee environments (Fig. 14). (B) CDF of set
 1080 thickness within bar stoss environments (Fig. 13). (C) CDF of thalweg set thickness (Fig. 15). The

1081 best-fit gamma and exponential curves are shown for each distribution. In all cases, the
 1082 exponential fits are rejected using a Kalmogorov-Smirnov test at a significance level of .05, and
 1083 the gamma fits are not. This suggests all architectures required a significant rate of bed
 1084 aggradation relative to the rate of dune migration, although the similarity of the two curves for
 1085 thalweg sets indicates the ratio of bed aggradation to dune migration was the lowest of the
 1086 three environments (Paola and Borgman, 1991; Jerolmack and Mohrig, 2005).



1087
 1088 Figure 19 – A diagram explaining the calculation of accumulation time (Eq. 2). The relative rates
 1089 of aggradation to migration are compared to deposit thickness, s , and an assumed dune
 1090 migration rate divided by the equivalent distance, m .

1091
 1092
 1093
 1094



1095

1096 Figure 20 – A diagram merging the observations of the usually bypass-state channel bed and
 1097 the relatively high amount of channel-bed aggradation preceding avulsion, when compared to
 1098 other fluvial strata (e.g., Mohrig et al., 2000). (A) at $t = 1$, the distance between the lowest part
 1099 of the floodplain and the channel bed (red line) during low flow is defined. (B) At $t = 2$, the
 1100 channel is in flood stage. The floodplain has aggraded less than the channel bed. Avulsion does
 1101 not occur. Original channel bed shown in red dashed line. (C) At $t = 3$, post-flood channel-bed
 1102 reworking fills scours and removes accumulations such that there is zero net change in bed
 1103 elevation.